An ant-inspired celestial compass applied to autonomous outdoor robot navigation

Julien Dupeyroux, Stéphane Viollet, Julien Serres

An ant-inspired celestial compass applied to autonomous outdoor robot navigation

Julien Dupeyroux, Stéphane Viollet, Julien R Serres*

Aix Marseille Univ, CNRS, ISM, Marseille, France

Abstract

Desert ants use the polarization of skylight and a combination of stride and ventral optic flow integration processes to track the nest and food positions when travelling, achieving outstanding performances. Navigation sensors such as global positioning systems and inertial measurement units still have disadvantages such as their low resolution and drift. Taking our inspiration from ants, we developed a 2-pixel celestial compass which computes the heading angle of a mobile robot in the ultraviolet range. The output signals obtained with this optical compass were investigated under various weather and ultraviolet conditions and compared with those obtained on a magnetometer in the vicinity of our laboratory. After being embedded on-board the robot, the sensor was first used to compensate for random yaw disturbances. We then used the compass to keep the Hexabot robot's heading angle constant in a straight forward walking task over a flat terrain while its walking movements were imposing yaw disturbances. Experiments performed under various meteorological conditions showed the occurrence of steady state heading angle errors ranging from 0.3° (with a clear sky) to 2.9° (under changeable sky conditions). The compass was also tested under canopies and showed a strong ability to determine the robot's heading while most of the sky was hidden by the foliage. Lastly, a waterproof, mono-pixel version of the sensor was designed and successfully tested in a preliminary underwater benchmark test. These results suggest this new optical compass shows great precision and reliability in a wide range of outdoor conditions, which makes it highly suitable for autonomous robotic outdoor navigation tasks. A celestial compass and a minimalistic optic flow sensor called M^2APix (based on Michaelis-Menten Auto-adaptive Pixels) were therefore embedded on-board our latest insectoid robot called AntBot, to complete the previously mentioned ant-like homing navigation processes. First the robot was displaced manually and made to return to its starting-point on the basis of its absolute knowledge of the coordinates of this point. Lastly, AntBot was tested in fully autonomous navigation experiments, in which it explored its environment and then returned to base using the same sensory modes as those on which desert ants rely. AntBot produced robust, precise localization performances with a homing error as small as 0.7% of the entire trajectory.

Keywords: Non-conventional vision, Optic flow, Hexapod, Homing, Odometry, Multiple sensory fusion, Bio-inspiration, Biomimetics, Bionics, Biorobotics

1. Introduction

Most autonomous navigation systems involve the use of Global Positioning System (GPS) and Inertial Measurement Units (IMUs). Unfortunately, the precision of civilian GPS is to within only a few meters, which makes them unsuitable for many robotic applications if they are not used in the differential mode. In addition, magnetometer measurements can be falsified by the local magnetic fields produced by ferrous materials in urban infrastructures. These magnetic disturbances have been classically compensated for using Kalman filtering methods, and the raw data provided by gyroscopes and accelerometers have to be fused [1]. The solutions proposed

*Corresponding author: Email address: julien.serres@univ-amu.fr

so far are still sensitive to disturbances of many kinds, since gyroscopes and accelerometers are also prone to drifts. The stakes involved in autonomous navigation include dealing with highly complex environments, where the magnetic fields are often unpredictable, and the precision of GPS is sometimes greatly reduced by the presence of buildings.

In this context, it seems likely that biomimetic approaches may yield some interesting alternative solutions. Here it was proposed to take our inspiration from the desert ants' skylight polarization compass [2] and their odometer [3] in order to provide robots with a reliable means of measuring their heading angle and the distance travelled when performing outdoor tasks.

The scattering of sunlight through the Earth's atmosphere produces a pattern of polarization across the sky [4]. Solar radiation remains unpolarized until entering the atmosphere, where scattering interactions with atmospheric constituents cause a partially linear pattern of polarization of the skylight [5] (Fig. 1). Along the solar and anti-solar meridians, the angle of the polarization is consistently perpendicular. However, as the Sun moves in the sky at an average speed of 15° per hour, the pattern of polarization is not constant, whereas its symmetry persists during the daytime.

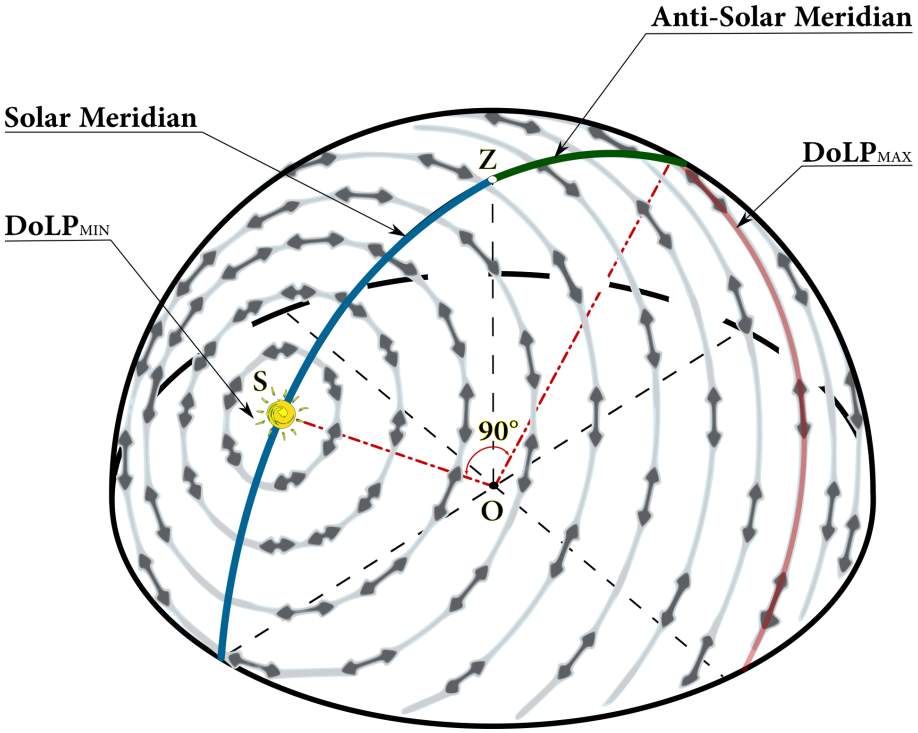

Figure 1: The linear pattern of polarization of skylight relative to the Sun (S) and an observer (O). Gray arrows give the angle of polarization of the skylight. The degree of linear polarization (DoLP) is given by the thickness of the arrows. The DoLP is minimum around the Sun (approximately 10% of skylight is linearly polarized), and maximum along the red curve at 90° from the Sun (approximately 90% [4]). The angle of polarization (AoP) is perpendicular to the solar (blue) and anti-solar (green) meridians.

Efficient navigation is crucial to foraging insects' survival. Insects such as desert ants *Cataglyphis* and *Melophorus* have two main systems of navigation: the path integration (PI) and landmark-based guidance (based on panoramic vision) systems [6]. PI has long been studied in desert ants [7, 8, 9]. Navigating ants make an egocentric estimate of their position, accumulating very few errors along their trajectory. Foraging desert ants never switch off their PI system, even when taking familiar routes [6], so that the insect is always connected to its nest, in the style of Ariadne's thread [10]. PI in desert ants is based on odometric and orientation-based navigation cues. The relevant odometric information is known to differ greatly among foraging insects. Flying insects such as flies and bees are thought to compute the distance travelled on the basis of either the optic flow (OF) [11] or snapshot images [12, 13]. Crawling insects base their travel distance information on stride integration processes and multiple visual cues, including the ventral [14] and panoramic OFs, the memorization of image snapshots [15], and the detection of the skyline [16].

PI in travelling desert ants *Cataglyphis* is now believed to rely only on ventral OF cues and stride integration processes [17]. In terms of orientation, entomological studies have shown the existence of ommatidia which are sensitive to the polarization of skylight in the Dorsal Rim Area (DRA) of insects' compound eye [18, 19]. The optical structure of each ommatidium makes it sensitive to a single angle of polarization (AoP), as well as to the corresponding orthogonal angle [20]. The spectral sensitivity of polarization is in the ultraviolet (UV) range in most navigating insects, but some species are sensitive to other wavelengths, including the blue and green ones [18]. During the past 40 years, several hypotheses have been put forward to explain the UV-predominance in insects' DRA (for a review, see [21]), but the most reasonable assumption seems to be that skylight polarization is clearly perceptible in the UV range even under canopies and clouds [22, 23]. The neural processing of polarized skylight in insects is thought to consist of three levels [24, 25]: (i) the relevant information is first acquired by the ommatidia in the DRA, without any preference for any specific AoP; (ii) in the second phase, the information is transmitted to the optic lobe, where polarization neurons (POL-neurons) show high levels of synaptic activity in response to three specific orientations (10°, 60° and 130°); (iii) lastly, the central complex uses the neural responses delivered by the optic lobe to retrieve the insects' heading (POL-neurons in the central complex produce a uniform synaptic response to all possible angles) [26].

Based on studies on the locust brain, Labhart developed a DRA-based model for estimating orientation, in which the logarithmic difference between the response of the ommatidium to a single polarization orientation and the response of the same ommatidium to the corresponding orthogonal polarization orientation is calculated [19]. Studies on the DRA in desert ants have shown that these insects refer to a single overall polarization angle to get their bearings [8]. For instance, during a foraging trip in an unknown place, desert ants *Cataglyphis* integrate their heading angle via their celestial compass. Although their foraging trip consists of a fairly random exploratory trajectory, their homing trajectory tends to take them straight back to the nest [8, 27].

Here we present a 2-pixel, UV-sensitive celestial compass for detecting the polarization of the skylight. The outstanding ability of this novel sensor to estimate the AoP was established in a wide range of outdoor conditions: under an open sky (with high to low UV-indexes, clear, changeable and overcast sky); under various tree canopies; in the presence of water droplets on the top of the sensor and immersed in water. The compass was first tested on-board Hexabot, one of the two hexapod robots presented here, in order to test its ability to make the robot keep to a fixed heading. In addition to the advantages of this celestial-based approach in comparison with traditional devices such as magnetometers, these abilities make this compass highly suitable for autonomous navigation purposes. A series of three navigation processes based on the desert ants' PI were therefore implemented and tested on-board the second robot, AntBot, equipped with a 12-pixel OF sensor. The results obtained show that a fully ant-inspired model, comprising celestial cues for controlling the heading and a combination of visual cues (OF) and proprioceptive (stride-counting) information for estimating the distance traveled, ensures that the robot will find its way back home with a low mean error of only 5.0cm $\pm$ 1.8cm, which is 70 times better than the 4.9m-accuracy of the civilian GPS. It was therefore clearly established that our PI-based navigation model is suitable for autonomous navigation purposes, providing a redundant source of information in addition to GPS, camera-based solutions and IMUs.

The research involved in this project is discussed in Section 2. The two insect-like robots, Hexabot and AntBot, used in this study are described and compared in Section 3. Section 4 describes the celestial compass, its computational model, its performances under various weather conditions, and those of which it is capable in the event of magnetometer failure in a real complex outdoor environment. The robots ability to track its heading is outlined in Section 5, while Section 6 describes the process of odometric cue acquisition with a 12-pixel OF sensor. Lastly, potential navigation applications are presented in Section 7, and the most noteworthy findings made in this study are discussed in Section 8.

2. Related research

The navigation ability of desert ants is far greater than that of their technological counterparts (such as GPS and IMUs) although their computational requirements are much lower and they show much greater robustness. These outstanding features inevitably led roboticists to develop and test insect-inspired strategies on mobile robots. On these lines, the first autonomous wheeled robot to use a celestial compass, Sahabot 1, was created by Lambrinos et al. in the late 1990s [28]. The spectral sensitivity of this compass inspired by the cricket's DRA ranged from $400nm$ to $520nm$. In the latter project, three modes of heading angle measurement were tested: (a) the scanning mode involved one pair of photodiodes topped with linear polarizers set orthogonally to each other, and made the robot turn around to find the orientation giving the strongest response, corresponding to the AoP (mean error: 1.73°). However, the rotating phase induced 2-D displacements and therefore increased the final position error induced when performing navigational tasks; (b) the extended scanning mode involves the same procedure as the scanning model but in this case, three polarization sensors are set at different orientations (0°, 60° and 120°), as in the optic lobe of insects (mean error: 1.16°). The angle of the solar meridian is then determined by simply subtracting the two sensor signals. This method provides more reliable results, since the peaks detected at the corresponding linear polarization angle are sharper than in the scanning model, but the 2-D drift is still an issue; (c) the simultaneous mode, in which three polarization sensors are used without rotating the robot. Logarithmic differences are computed between each sub-unit of the POL-sensors so that the heading angle can be accurately estimated. Tests were performed in the early morning and the mean angular error was 0.66° using the simultaneous mode, and 1.73° using the simple scanning mode. The simultaneous model was therefore applied to Sahabot 2 in order to implement ant-inspired PI processes (mean homing error: 13.5cm in the case of a trajectory of 70m), and test panoramic vision-based models [29]. It is still not clear how insects distinguish between solar and anti-solar angles, but some authors have suggested that insects may use a circadian clock to both dispel the heading angle ambiguity and compensate for the Sun's path [10], while some others have suggested that the solar ambiguity may be solved by the POL-neurons by matching the polarization pattern with a specific solar position (matched filters) [30]. Sahabot simply integrated the position of the Sun to prevent the occurrence of any ambiguity [28, 29].

Authors	Year	Ref.	Technological solution	Insect-based	UV	Minimalistic	Rotating filters
Lambrinos et al.	1997	[28]	Photodiodes	✓	×	✓	×
Chu et al.	2008	[31]		✓	×	✓	×
Chahl et al.	2012	[32]		✓	×	✓	×
Wang et al.	2015	[33]		×	✓	×	×
Zhi et al.	2018	[34]		×	×	✓	×
Dupeyroux et al.	2019	[35]		✓	✓	✓	✓
Sarkar et al.	2010	[36]	Integrated pol. sensor	×	×	×	×
Chu et al.	2014	[37]		✓	×	✓	×
Garcia et al.	2017	[38]		Crustacean	×	×	×
Carey et al.	2011	[39]	Camera-based	✓	✓	×	×
Sarkar et al.	2013	[40]		✓	×	×	×
Wang et al.	2014	[41]		✓	×	×	×
Zhang et al.	2015	[42]		✓	✓	×	×
Fan et al.	2016	[43]		×	×	×	×
Zhang et al.	2016	[44]		×	✓	×	×
Wang et al.	2017	[45]		×	×	×	×
Han et al.	2017	[46]		×	×	×	×
Fan et al.	2018	[47]		×	×	×	×
Momeni et al.	2006	[48]	VLSI	×	×	×	×

Table 1: A non-exhaustive classification of celestial compasses. The minimalism of a solution depends on the number of photoreceptors that form a celestial compass: the technological solution is taken to be minimalistic if it comprises at most a few dozens of photoreceptors.

Chu et al. recently developed a celestial compass based on that integrated into the Sahabot projects using the simultaneous mode [31, 49], which gave a mean homing error of 42cm (in the case of a complete trajectory 32m long). The optical compass was mounted on-board a wheeled robot, using a fuzzy logic controller to make it follow a pre-programmed trajectory. Tests were performed at the end of the day in order to prevent the occurrence of any sensor saturation. A miniaturized version of the celestial compass has also been presented (giving a mean angular error to within $\pm 0.1^{\circ}$) [37].

Another version of the celestial compass has been mounted on a small Unmanned Aerial Vehicle (UAV) [32]. Three polarization sensors giving the effective angles and their corresponding orthogonals were integrated into an ocelli-based autopilot designed to control the UAV's roll and pitch during ten seconds of flight [32]. In 2018, an attitude determination system including a polarization sensor was built and embedded on-board a quadrotor UAV [34], giving a more accurate method of autonomous navigation. As far as the present authors know, no other PI-based strategies have been implemented and tested so far on-board mobile robots.

Among the many studies which have been conducted on the design and use of celestial compasses, whether insect-inspired or not, some authors have used only a few photodiodes while others have used one or more cameras, and most of these compasses have acquired polarization cues in the visible range rather than the UV-range (see Table 1 for references). To this day, no further robotic implementations of desert ant-inspired sensors and PI methods have surpassed Sahabot's impressive results (mean homing error: 13.5cm). As in the case of visual-based navigation, the present models still have to deal with some persistent issues. Due to the large number of pixels (usually several megapixels) usually required and the varying complexity of the algorithms involved, in addition to the fact that the data have to be integrated with the information delivered by other sensors such as GPS and IMUs, the high computational cost has become a critical factor. In addition, most commonly available visual sensors are highly sensitive to ambient light changes in outdoor settings. Lastly, it is generally difficult to embed these visual systems on-board small robots (not to mention the need to stabilize the cameras against attitude disturbances).

In view of the great potential of PI, it was proposed to develop a new version with which to equip hexapod robots, mimicking insects' locomotor processes using the minimalistic sensors we developed to enable these robots to perform homing navigation tasks with much greater precision and robustness than any of the systems previously presented in the literature. The methods proposed here require only 14 pixels distributed between two sensors: two pixels covered with rotating polarized filters, thus equivalent to two arrays of 374 pixels, deal with the acquisition of the heading angle, while the other 12 are devoted to odometric calculations.

3. AntBot and Hexabot, the insect-like robots

The two fully open-source, 3D-printed, six-legged insectoid robots we have built mimic the desert ant's performances of several navigational tasks such as homing in unknown environments. The first robot, which was called Hexabot and has been presented in detail in [50] (Fig. 2Top), was used in the first few experiments described in this study. Unfortunately, due to the weakness of its actuators, it was not possible to plan to make Hexabot travel long distances. We therefore constructed the AntBot robot (Fig. 2Middle), giving it the same architecture as Hexabot but more powerful actuators, and used it to perform the second series of experiments in this study.

The overall weight of Hexabot, including the batteries, is 925g, and the maximum length is 360mm, while the maximum height of the centre of mass is 145mm. Depending on the capacity, the battery life ranges from half an hour to one hour. The robot has three Dynamixel XL-320 actuators per leg, which enable it to reach high walking speeds (approximately 35cm/s under optimum conditions). These six-legged robots show more stable walking performances than the previous four-legged ones since they can make use of static gait (i.e. three to five legs can remain on the ground at any given time). Hexabot's walking gait and drift on flat terrain were analyzed. Ground truth measurements were performed using the 17 motion-capture cameras (VICON™)

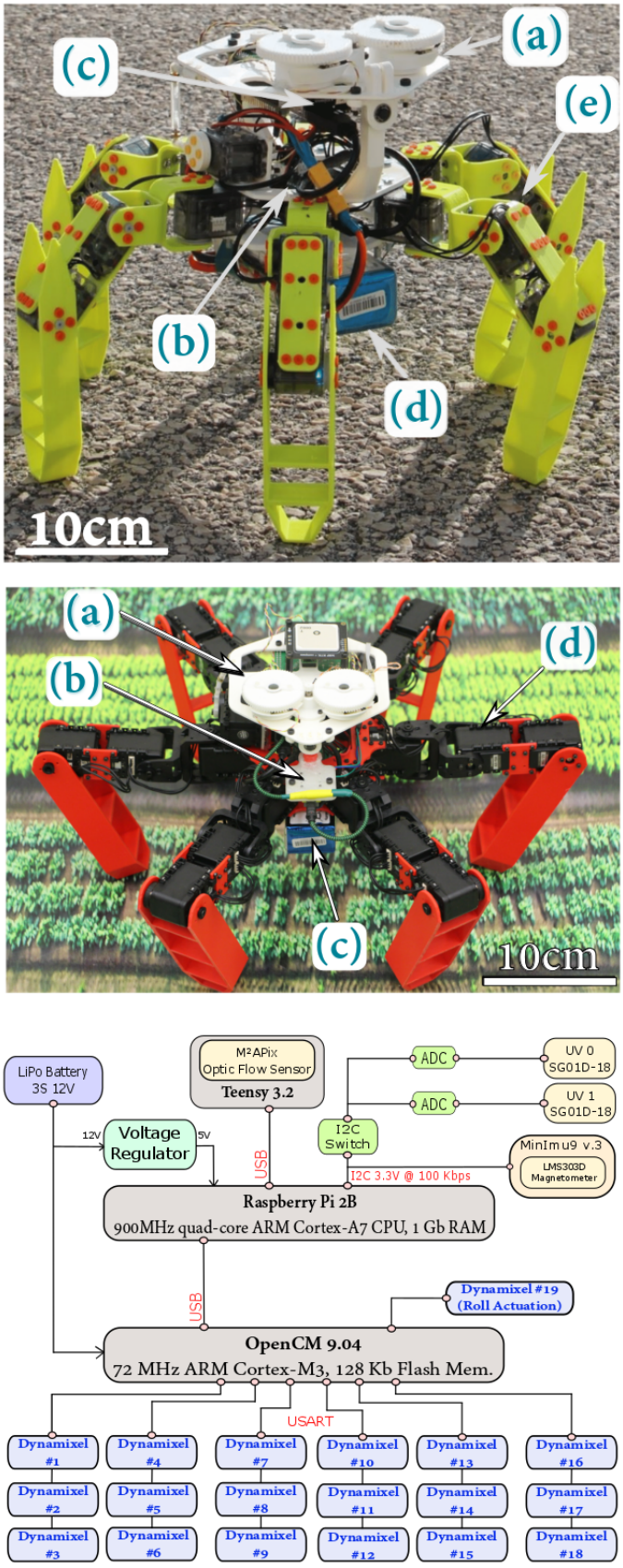

Figure 2: **Top** Hexabot equipped with the 2-pixel celestial compass (a). The robot is controlled by an OpenCM 9.04C (b), and its high-level navigation is processed in the Raspberry Pi2B board (c). The 11.1V 2500mAh battery (d) is mounted below the robot. (e) Dynamixel XL320 servomotors. Adapted from [51]. **Middle** AntBot equiped with the celestial compass [52] (a) and the ventral OF sensor [53, 54] (b). The 11.1V 5300mAh lithium polymer battery (c) is placed below the robot. (d) Dynamixel AX18 servomotors. **Bottom** General hardware architecture of the Hexabot and AntBot robots. The M^2APix optic flow sensor is mounted on-board AntBot. The 19^{th} servomotor is used to actuate the robot's head around the roll axis to disambiguate the solar/anti-solar uncertainty affecting the determination of the AoP.

	Size	Weight	Autonomy	Actuators	Max. speed	Lat. drift	Roll	Pitch
Ants	5 - 18mm	<0.15g	-	-	70cm/s (40b-l/s)	-	10°	60°
Hexabot	360mm	925g	60min	XL-320	35cm/s (1b-l/s)	34cm	9°	9.9°
AntBot	450mm	2300g	30min	AX-18A	90cm/s (2b-l/s)	-	-	-

Table 2: Comparison between Hexabot and AntBot robots. The lateral drift is the robot's average lateral displacement when it was made to walk straight forward for one meter at maximum speed. Roll and pitch values are the average angular disturbances occurring during straight forward walking at maximum speed on a flat terrain. Speeds are also given in body lengths per seconds (b-l/s). Ants' characteristics are typical values available in the literature on desert ants *Cataglyphis* and *Melophorus*; these performances are given for the sake of comparison.

with which the Flying Arena of the Mediterranean is equipped[1] (6m x 8m x 6m-height) [50]. Hexabot's performances showed small mean roll and pitch disturbances of about 9.0° and 9.9°, respectively, when tested at maximum speed (Table 2), whereas Hexabot's yaw orientation was greatly disturbed (up to 28.4°), which caused considerable drift from the initial trajectory.

AntBot[2] is a larger version of Hexabot (it is 45cm wide and weighs 2300g) which is able to house Dynamixel AX-18A servomotors, which are larger and more powerful than the XL-320 ones. AntBot's maximum speed measured under optimum conditions was found to be about 90cm/s. Although the same firmware was used in AntBot as in Hexabot, its actuators seem to make its walking gait more stable. However, its long-term navigation performances are still subject to considerable yaw drift, which will have to be corrected. AntBot's maximum autonomy amounted to 30 minutes when a 11.1V 5300mAh lithium-polymer battery was used. Detailed comparisons between Hexabot and AntBot are made in Table 2, including with desert ants' corresponding performances.

These robots are controlled by an OpenCM9.04C micro-controller (32-bit ARM Cortex-M3). This first control board is connected to a second one, a Raspberry Pi 2B board (32-bit quad-core ARM Cortex-A7), which is responsible for sensor data acquisition and processing and sends high level orders to the robot's main controller (Fig. 2Bottom). The celestial compass is embedded on the dorsal part of the robot (element (a) in Fig. 2Top and 2Middle). Communications with the Raspberry Pi board were implemented using I2C protocol. The general electronic architecture is presented in Fig. 2Bottom.

4. The ant-inspired celestial compass

4.1. The UV-polarized light sensor

As shown in Fig. 3A-B, the celestial compass is composed of two UV-light sensors (Sg01D18, SgLux, spectral sensitivity within the [200;375]nm range), topped with UV linear sheet polarizers (HNP'B replacements with a spectral sensitivity ranging between 270nm and 750nm). The polarizers are placed on rotating gears actuated by a stepper motor (AM0820-A-0225-7, Faulhaber). The reduction gear ratio is 7:1. The sensor's angular resolution was set arbitrarily at 1.29° in the experiments conducted with Hexabot (acquisition time: 42 seconds), and 0.95° in those performed with AntBot (acquisition time: 20 seconds thanks to software improvements). The celestial compass was 3-D-printed[3] using polylactic acid (PLA). The two photodiodes topped with linear polarizers are referred to here as POL-units. As in the polarized-sensitive photodetectors found to occur in desert ants *Cataglyphis*, the two polarizers are set perpendicularly to each other here. The left and right POL-units are denoted by UV_0 and UV_1, respectively. x is taken to denote the rotation angle, in degrees ($x \in [0;360]^\circ$), of the UV polarizers, and Ψ is the solar meridian angle computed by the celestial compass ($\Psi \in [0;180]^\circ$).

[1] More information at: http://www.flying-arena.eu.

[2] AntBot's 3-D parts are available at: https://github.com/JuSquare/AntBot/tree/master/3D Parts.

[3] The parts are available at: https://github.com/JuSquare/AntBot/CelestialCompass.

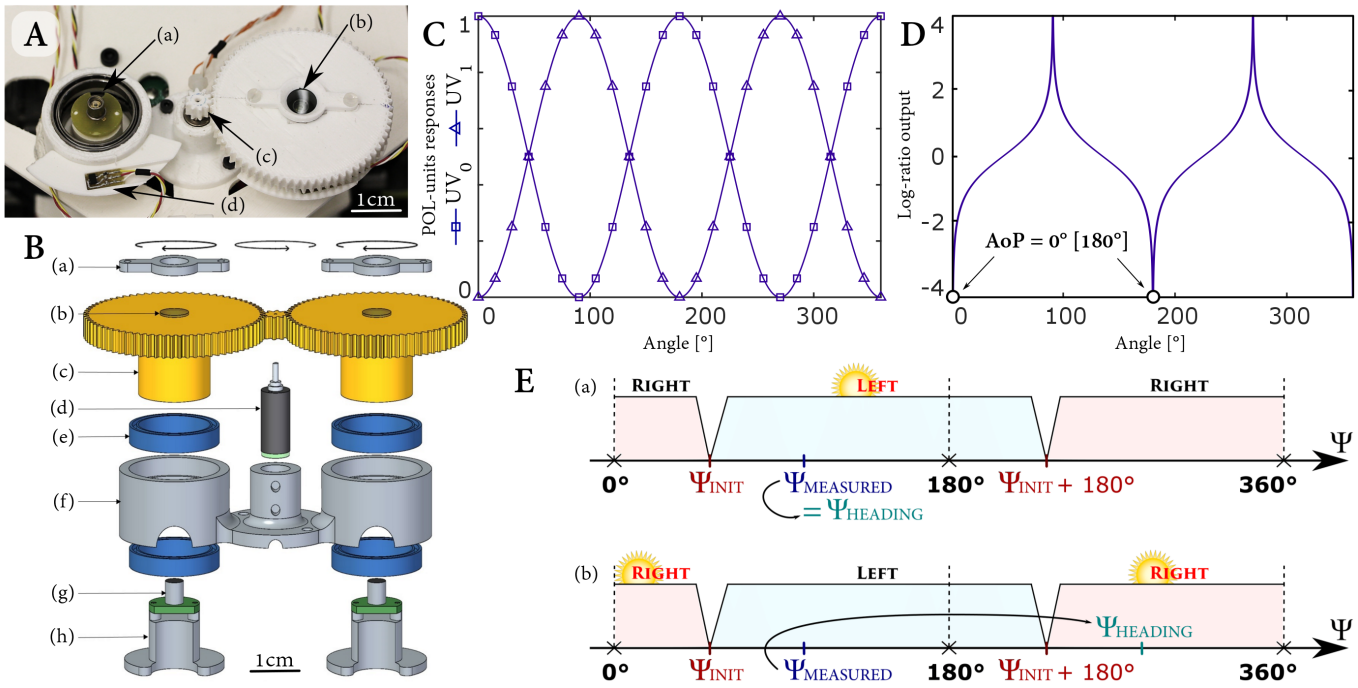

Figure 3: The celestial compass. **A** Photograph of the 3-D-printed celestial compass mounted onboard Hexabot and AntBot. (a) UV light sensors. (b) Linear sheet polarizer. (c) Stepper motor. (d) Hall-effect sensor. Printing material: polylactic acid (PLA). **B** Exploded computer-aided design (CAD) view of the celestial compass. (a) Fixation support for the polarizers. (b) UV linear sheet polarizers (HNP'B replacements, spectral sensitivity: 270nm - 750nm with a peak transmission at 330nm with a transmittance of 50%). (c) Rotating gears. (d) Stepper motor (AM0820-A-0225-7, Faulhaber). (e) Main compass frame. (f) Ball bearings. (g) UV-light sensors (Sg01D18, SgLux) with a spectral sensitivity ranging from 200nm to 375nm, and peak response at 280nm for which the polarizer's transmittance is equal to 24%. (h) Fixation support for the photodiodes. **(B)** Assembled CAD view of the celestial compass. **C** Typical normalized and filtered responses at an angle of polarization (AoP) of 0°. **D** Corresponding log-ratio function. **E** Solar-based solution to the heading ambiguity. (Top) The $\Psi_{MEASURED}$ acquired was located in the same angular sector as the Sun, resulting in $\Psi_{HEADING} = \Psi_{MEASURED}$. (Bottom) The Sun was located to the right of the robot, while the heading angle $\Psi_{MEASURED}$ is on the left. $\Psi_{HEADING} = \Psi_{MEASURED} + 180°$. Ψ_{INIT} is therefore the robot's initial heading angle, which is acquired/recorded at the beginning of each experiment, and is always assigned to the first angular interval $[0;180]°$.

The strategy proposed here consisted of combining the scanning and simultaneous modes presented by Lambrinos *et al.* [28] into a UV-polarized light scanning model giving highly accurate measurements for our walking robot's heading angle under various weather conditions and with low UV indexes. The scanning model meant that the robot had to turn by 360° to complete the data acquisition. Although this model is advantageous as it yields a larger number of measurements for determining the AoP, the turning motion of the robot adds the risk of position drift, which would be deleterious in the case of real-life navigation. Our celestial compass uses rotating filters set on top of the photodiodes to perform time-multiplexing measurements without having to make the robot move. This solution is consistent with the distribution of the ommatidia in the DRA of desert ants' compound eye.

The POL-units' responses presented in Fig. 3C correspond to the UV photodiodes' signals obtained by rotating the linear polarizers by 360°. Both POL-units UV_0 and UV_1 can therefore be expressed as follows:

$$\begin{cases} UV_0(x) = A_0 + B_0 \cdot cos(2(x + \Psi)) \\ UV_1(x) = A_1 + B_1 \cdot cos(2(x + \Psi + 90°)) \end{cases} \quad (1)$$

Constants A_0 and A_1 are offsets depending on both the ambient UV-light and the inner bias of each POL-sensor. Likewise, constants B_0 and B_1 depend on both the degree of linear polarization (DoLP) and the inner gain of each POL-sensor. According to the algorithm 1, each POL-unit's response is first low-pass filtered (only the static and first harmonic components are kept) and then

normalized between ϵ and 1, where $\epsilon \ll 1$ is set so as to prevent logarithmic computation failure. The normalized and corrected POL-units' outputs are denoted by UV_0^{nc} and UV_1^{nc}, respectively. The log-ratio function $p(x)$ is defined as follows (Fig. 3D):

$$p(x) = log_{10}\left(\frac{UV_1^{nc}(x)}{UV_0^{nc}(x)}\right) \tag{2}$$

Algorithm 1 Low-pass filtering and normalization of UV_0 and UV_1 signals. ***fft*** and ***ifft*** are the direct and reverse fast Fourier transforms, respectively, and $\epsilon = 0.0001$.

1: **for** i$\in [0:1]$ **do**
2: $\quad \widehat{UV_i} = \boldsymbol{fft}(UV_i)$
3: $\quad \widehat{UV_i}[3 : length(\widehat{UV_i}) - 3] = 0$
4: $\quad UV_i^n = \boldsymbol{abs}(\boldsymbol{ifft}(\widehat{UV_i}))$
5: $\quad UV_i^{nc} = UV_i^n - min(UV_i^n) + \epsilon$
6: $\quad UV_i^{nc} = UV_i^{nc} / max(UV_i^{nc})$
7: **end**

We then computed the solar meridian angle Ψ by locating the two minimum local values of the p function, the first of which is in the d$[0;180]^\circ$ range and the second one, in the $[180;360]^\circ$ range (Fig. 3D):

$$\Psi = \frac{1}{2}\left(\underset{x\in[0;180]^\circ}{\arg\min}\, p(x) + \underset{x\in[180;360]^\circ}{\arg\min}\; p(x) - 180^\circ\right) \tag{3}$$

Due to the symmetry of the pattern of polarization around the zenith point, Ψ is only known to within $[0;180]^\circ$. The methods classically used to eliminate the ambiguity between Ψ_{Solar} and $\Psi_{Anti-Solar}$ take the ambient radiance distribution, which is determined by means of either a set of photodiodes [29] or a camera oriented toward the zenith of the sky dome. Here we decided to roll the celestial compass left and right. In each case, the UV light intensity was determined by adding the two photodiodes' measurements (UV_0 and UV_1). The part of the sky corresponding to the highest UV level is therefore that which contains the Sun. This procedure can be used to solve most ambiguity issues. In the case where the UV level is practically the same on both the robot's left and right sides (i.e., when the Sun is aligned with the robot's longitudinal axis), the solar ambiguity is solved by the turning stride integrator. The solution to the solar-based ambiguity problem is presented graphically in Fig. 3E.

4.2. Performances of the celestial compass under various weather conditions

The aim of this section is to show how well the celestial compass performs under all weather conditions (with a clear, changeable and covered sky) [35]. The benchmark test used in this study consisted in rotating the celestial compass by 10° from 0° to 170° in an outdoor area. At each rotating step, a full acquisition of the polarized skylight was performed with the celestial compass and the AoP was retrieved based on (3). The data were collected from February to June 2017 in Marseille, France (43°14'01.16"N, 5°26'39.2"E). During this 5-month period, the UV-index ranged from 1 to 8 (source: European Space Agency and the Tropospheric Emission Monitoring Internet Service). During the acquisition phase, the sun's course was compensated for based on the solar ephemeris data giving the date, time (CET and CEST) and location of the experiments. Three different weather conditions were tested here: (i) the clear sky condition, where absolutely no clouds occurred in the sky; (ii) the changeable sky condition, where clouds occurred randomly in the sky, sometimes hiding the sun; (iii) the covered sky condition, where the sky was completely overcast. The experiments took place at all times of the day between 9:00am and 6:00pm.

The angular errors recorded under all weather conditions are given in Table 3. None of the angular error distributions showed a normal distribution (Shapiro-Wilk normality test, p-value

	Clear sky *(n=180)* UV-index: 5.6 ± 1.3	Changeable sky *(n=180)* UV-index: 5.8 ± 1.2	Covered sky *(n=108)* UV-index: 3.0 ± 0.0
Mean	0.69°	9.55°	17.98°
Median	0.39°	0.02°	0.59°
SD	0.52°	4.81°	9.81°
C_v	0.75	0.50	0.55

Table 3: Angular errors of the AoP computation method under various sky conditions (clear, changeable and covered). SD: standard deviation. UV values are dimensionless and expressed as means $\pm$ SD. n is the number of data, defined as the number of experiments multiplied by 18, corresponding to the number of data collected during each experiment. C_v is the coefficient of variation ($C_v = SD/Mean$).

< 0.05). Under clear sky conditions, the angular error between the heading estimated with the celestial compass and the ground truth was always very low, with a median value of 0.39° and a low variability as the standard deviation amounted to only 0.52°. The angular error reached mean values equal to $9.55° \pm 4.81°$ and $17.98° \pm 9.81°$ under changeable and covered sky conditions, respectively, whereas the median value was always less than 1°.

It is worth noting that all the median values obtained were below the angular resolution of the celestial compass, which was set at 0.96° in these experiments. In addition, the coefficient of variation C_v, which is equal to the ratio between the standard deviation and the mean value, was consistently stable although the weather varied from a clear to a fully covered sky (Table 3). These two findings establish the weather-resilience of this 2-pixel celestial compass in the UV-range, and suggest that it has a high potential for use in autonomous navigation tasks.

4.3. Performances of the celestial compass under canopies

Here we established the ability of our celestial compass to detect the AoP under two typical Mediterranean trees growing in Provence (Southern France), namely Judas trees (*Cercis siliquastrum*), and downy oaks (*Quercus pubescens*). The robot was placed on the ground below the canopy, looking up toward the zenith. The robot's heading was determined in the case of three different orientations: 0°, 60° and 120°. Several data acquisition runs were performed in the afternoon during summer 2018 in Marseille, France. The UV-index ranged from 7 to 10.

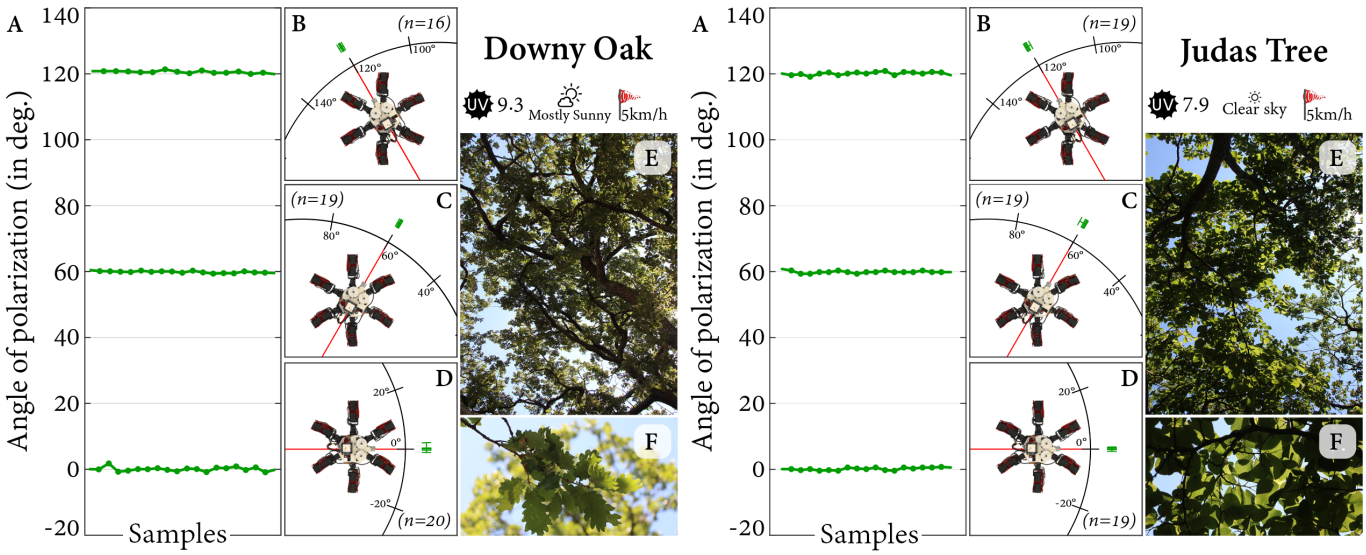

Figure 4: The AoP determined under typical Mediterranean canopies: downy oaks (left) and Judas trees (right). **A** Estimated angle in degrees. **B-D** 2-D picture of the experiment, giving an angular boxplot of the estimated heading. **E** Photograph of the sky. **F** Magnified view of the leaves showing the extent to which the visual field was obstructed. The weather conditions (UV-index, sky conditions and wind) are specified in the case of each canopy.

The headings calculated are shown in Fig. 4, and the statistical results are presented in Table 4. Under different canopies, the celestial compass was able to correctly estimate the AoP with an

overall error equal to $0.08^\circ \pm 0.54^\circ$ under downy oaks ($n = 55$) and $-0.02^\circ \pm 0.47^\circ$ under Judas trees ($n = 57$), respectively. The normality of the angular error distributions was also checked by applying Lilliefor's normality test ($P > 0.05$). These results are consistent with the previous performances of the compass obtained under an open sky. The substantial increase in the accuracy may have been due to the presence of higher UV-index (open sky: UV-index < 6.0; under canopies: UV-index > 8.0). However, it seems likely that the presence of foliage above the compass does not affect the AoP in the UV. This hypothesis has been previously put forward by Barta and Horváth [23] to explain the prevalence of the UV-preference in the processes used by insects to detect the polarized skylight in order to use it as a navigational cue.

	Downy Oak				Judas Tree			
	Median	Mean	SD	n	Median	Mean	SD	n
0°	0.04°	0.00°	0.64°	20	0.00°	0.00°	0.35°	19
60°	59.88°	59.84°	0.32°	19	59.74°	59.84°	0.55°	19
120°	120.50°	120.48°	0.40°	16	120.14°	120.11°	0.47°	19
Overall error	0.06°	0.08°	0.54°	55	0.00°	-0.02°	0.47°	57

Table 4: Estimation of the AoP under downy oaks and Judas trees.

4.4. Underwater performances

It was proposed here to investigate the potential underwater applications of this compass to measure the polarized skylight for navigation purposes. Two sets of experiments were performed: in the first ones, the effects of placing a single droplet of water on top of the compass to simulate rain were analyzed; it was then proposed to determine how visible the linearly polarized skylight was to the compass underwater.

In 1954, T. Waterman proved that the polarized pattern of the skylight is still visible under water at depths of up to 200m [55]. However, the possible applications of using these celestial cues underwater for navigation purposes have long been a subject of debate, especially as a misconception has arisen in the scientific community that most of the polarized light detected under water is polarized horizontally and therefore cannot be used as a navigation cue [56, 57]. In the latter study, T. Waterman established that the underwater celestial pattern of the skylight is similar to that observed in the air (Fig. 5A) [57]. In addition, some marine animals have turned out to be able to perceive and use the polarized light to orientate themselves [58, 59, 60]. We designed a mono-pixel waterproof version of the celestial compass (Fig. 5B). This compass corresponds basically to one POL-unit, consisting of a UV-sensitive photodiode topped with a linear polarizer. This POL-unit was encapsulated inside a custom-made casing that was waterproofed using epoxy resin. This package was then fixed onto a stepper motor (a standard motor removed from a printer). The angular resolution was set at $360^\circ/400 = 0.9^\circ$. The AoP was then computed based on (3), where the UV_0^{nc} signal corresponds to the normalized and filtered signal acquired by the mono-pixel compass and the UV_1 signal is equal to $1 - UV_0^{nc}$.

4.4.1. Simulating rain

This first set of experiments was defined with a view to: (i) determining whether the presence of a water droplet on the polarized filter might disturb the measurement of the heading in comparison with the situation with no droplets; (ii) checking the consistency of the heading estimation with the water droplet by comparing the estimations at two arbitrarily fixed orientations 90° apart. The data were collected during September 2019 under clear sky conditions with a UV-index of approximately 6.0.

With and without a water droplet. A series of 18 acquisitions were performed without the water droplet at a fixed orientation. We then placed a water droplet on top of the compass and carried out 12 other data acquisitions without changing the orientation of the sensor. The experiment took 15 minutes between 3:30pm and 3:45pm, which corresponded to an angular drift of the

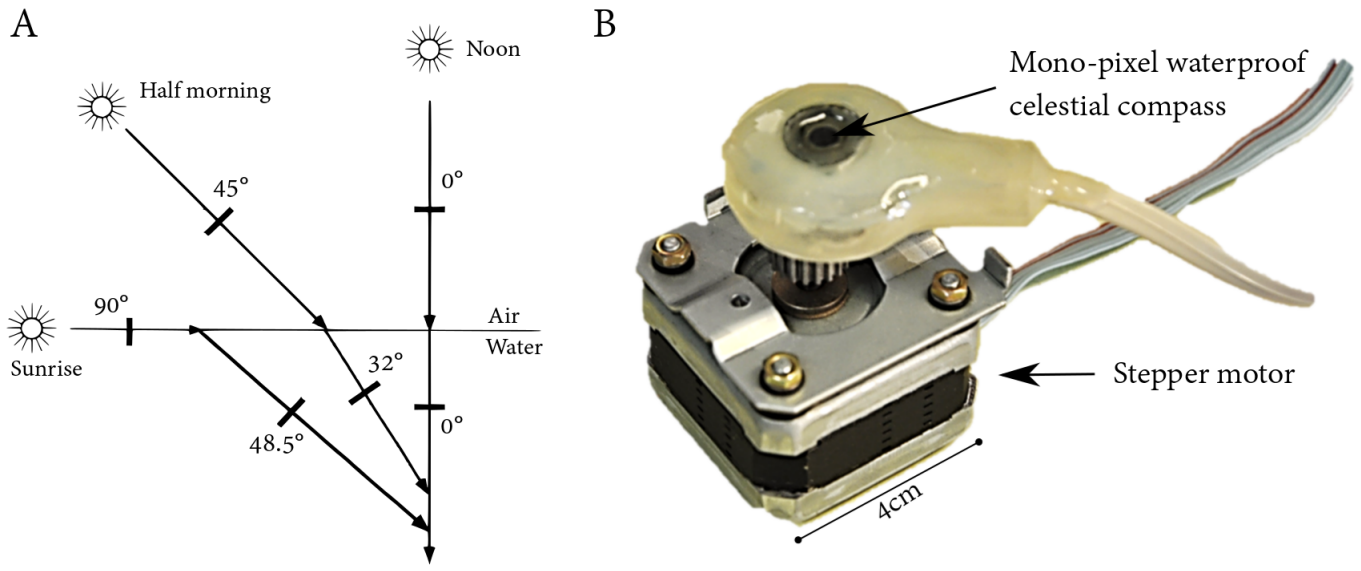

Figure 5: **A** Simplified diagram showing the effects of the air/freshwater interface on the propagation of the polarized skylight, depending on the solar elevation and for wavelenghs in the visible range. Adapted from [57]. **B** Mono-pixel celestial compass composed of one UV-sensitive photodiode topped with a UV-transmitting linear polarized filter. The sensor was encapsulated in a custom-made waterproof casing covered with epoxy resin.

Sun's elevation of 2.34°. The normalized and filtered signals and their corresponding log-ratio functions (2) are given in Fig. 6.

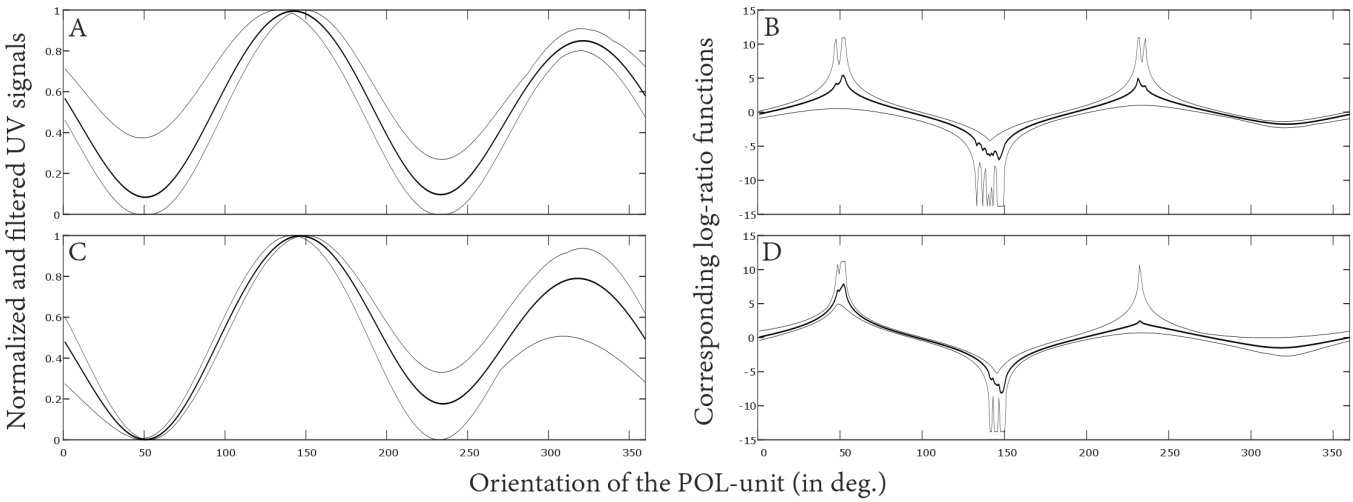

Figure 6: Signals obtained with the mono-pixel celestial compass in the case of simulated rain. **A** Normalized and filtered signals obtained under dry conditions ($n = 18$). **B** Corresponding log-ratio function. **C** Normalized and filtered signals obtained in the presence of the water droplet ($n = 12$). **D** Corresponding log-ratio functions. Thick lines stand for the mean signals; thin lines give the maximum and minimum curves.

The dry condition yielded a heading angle equal to $142.2° \pm 2.33°$ (mean $\pm$ *sd*). When the water droplet was placed on the compass, the estimated heading was equal to $143.9° \pm 2.09°$. The distributions of the heading angles under both dry and wet conditions are presented in Fig. 7. The median of angles distributions were therefore equal to 144.0° and 144.5°, respectively. The wet RMSE ϵ_{water} was calculated taking the dry condition as the reference condition (4), resulting in an angular error $\epsilon_{water} = 2.62°$.

$$\epsilon_{water} = \sqrt{\frac{1}{n} \cdot \sum_{i=1}^{n} \left(\bar{\psi}_{dry} - \psi_{water}[i]\right)^2} \tag{4}$$

Given the 2.34° angular drift of the Sun during the experiment, the presence of the water droplet can be said to have had not effect on the heading angle estimation. This has been statis-

tically confirmed through a Wilcoxon test using the *ranksum* Matlab function, showing there is no significant difference between the two distributions ($P > 0.05$). Since these results are highly encouraging, it might be worth developing a waterproof version of the celestial compass for navigating in rainy weather. However, the experimental conditions tested here differ from reality because they did not include an overcast sky. Based on recent findings on the performances of the celestial compass under a covered sky, the presence of clouds can be expected to have a slight impact on the sensor's real-life performances [35].

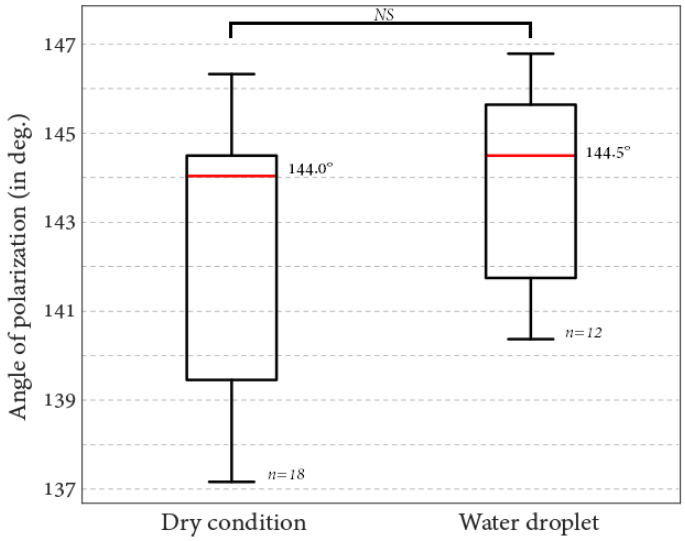

Figure 7: Boxplots showing the distribution of the angles of polarization determined under dry (left) and wet (right) conditions.

With a water droplet: the consistency of the heading estimates. After placing a water droplet on top of the sensor, two series of data acquisitions were performed at orientations 90° apart. At the first arbitrarily fixed orientation, the heading was equal to $146.9° \pm 0.96°$ ($n = 9$). After shifting the orientation of the mono-pixel celestial compass by 90°, the AoP computed was found to be equal to $56.0° \pm 2.69°$ ($n = 10$). The RMSE recorded taking the first orientation as the reference value was equal to $-90.91°$. The acquisitions lasted for 5 minutes, during which time an angular drift of the Sun's elevation of 0.8° occurred. The angular gap found to occur between the two sets of experimental data was therefore consistent with the 90° shift of the celestial compass, which shows that the AoP would be a reliable heading cue under rainy weather conditions. Again, statistical investigations with the Wilcoxon test showed that the two datasets (i.e. the first one and the second one for which we added 90° for each AoP) were not significantly different ($P > 0.05$).

4.4.2. Underwater signal detection

Here we focus on the ability of the mono-pixel celestial compass to compute the AoP when placed at the bottom of a water tank. Although it is rather difficult to perform outdoor underwater experiments, we managed to carry out 4 data acquisitions. The water tank used had a volume of $1m^3$ (dimensions: 1m x 1m x 1m). The experimental set-up is displayed in Fig. 8A-C. The angular field of view was 52°. The data were obtained under a clear sky in September 2019. The signals (POL-unit and log-ratio) are plotted in Fig. 8D-F.

The results presented here were obtained at a given fixed orientation of the celestial compass. The angles of polarization computed were equal to: $-4.9°$, 2.3°, 3.2° and 3.6°, giving a mean value of $1.0° \pm 4.0°$. These preliminary results suggest that the celestial pattern of polarization detected under freshwater could be used, at least at low depths, without any major differences with the measurements performed in the air.

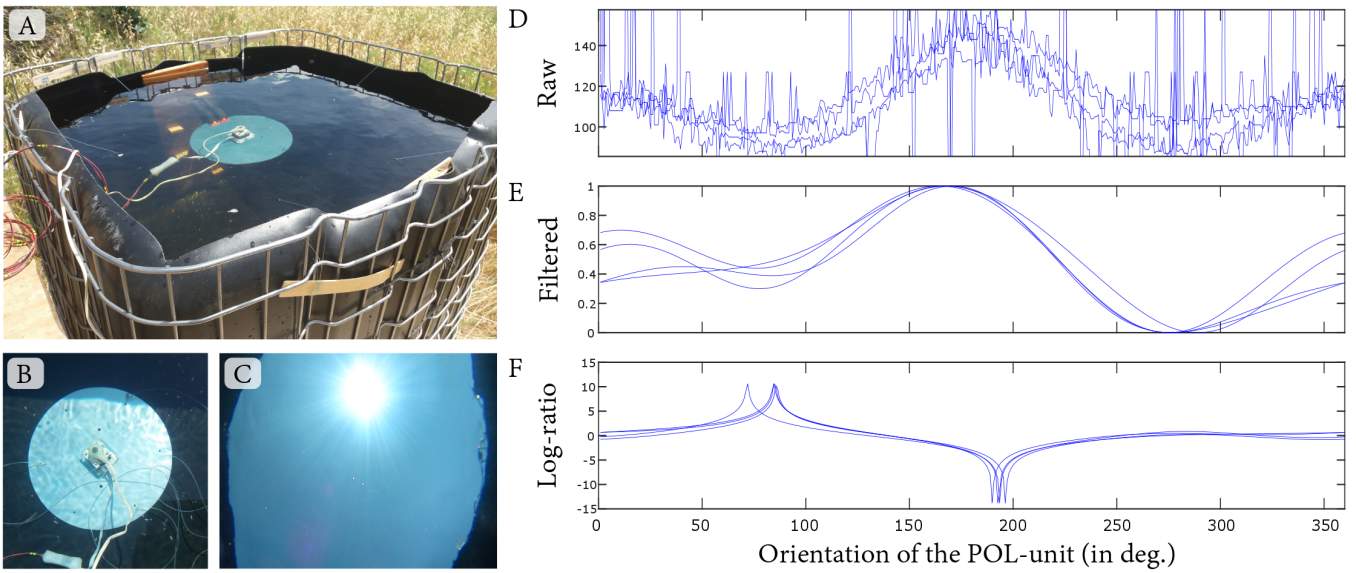

Figure 8: Underwater experiments. **A-C** Photographs of the set-up. **D** Four distinct raw signals obtained with the mono-pixel celestial compass. **E** The four POL-unit signals after filtering and normalization. **F** The corresponding log-ratio signals.

4.5. Celestial compass vs. Magnetometer

In outdoor navigation, most traditional methods have involved the use of magnetometers to determine the heading angle of a mobile robot. However, navigation in cities is complicated by the unpredictable magnetic fields generated by the ferrous materials used in present-day buildings. It was therefore proposed to show how reliable and precise the celestial compass is as a means of estimating the orientation in comparison with classical magnetometers (MinIMU9 v3, LMS303D). Nine experiments were performed in the vicinity of our campus, where the magnetic fields greatly disrupted the magnetometer, from April to June 2017 with UV indexes ranging from 7 to 9 (Fig. 9A. In each experiment, the robot was placed on a rotating table and turned in 10° steps until a complete rotation was achieved. The results are presented in Fig. 9B.

The RMSE between the theoretical and computed angles of the heading angle, denoted η_k ($k \in [\![1..9]\!]$), is defined in (5), where $\widehat{\Psi}$ is the heading angle computed with either the magnetometer or the celestial compass. Statistical results are given in Table 5.

$$\eta_k = RMSE(\widehat{\Psi}) = \sqrt{\frac{1}{36}\sum_{i=1}^{36}\left(\widehat{\Psi(i)} - 10 * i\right)^2} \tag{5}$$

Sensor	$\overline{\eta}$	σ
Celestial Compass	2.5°	0.7°
Magnetometer	59.1°	1.7°

Table 5: Mean celestial compass and magnetometer values $\overline{\eta}$ and standard deviations σ of the RMSE results under clear sky conditions (UV-index$\in [7;9]$).

The mean angular error produced by our celestial compass clearly confirms that this ant-inspired sensor can be used in outdoor environments to back up the magnetometer in the event of strong magnetic disruptions.

5. Determining the heading angle on-board the Hexabot robot

The aim of the first series of experiments was to establish how precise and robust the celestial-based estimates of the robot's heading angle are. Tests were conducted between 02/02/2017 and

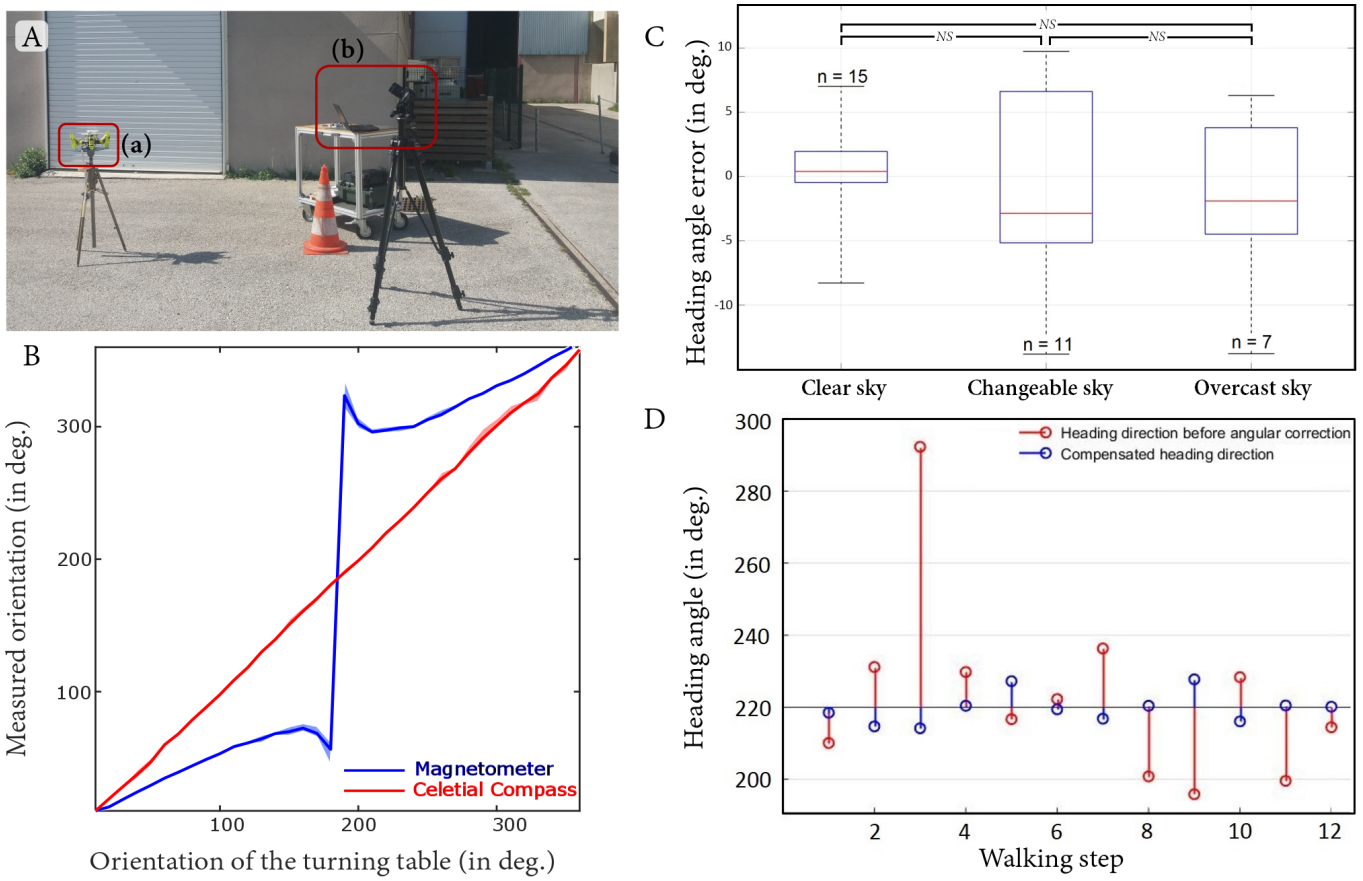

Figure 9: **(A)** Experimental context in front of our laboratory: (a) Hexabot equipped with the celestial compass; (b) the host computer. **(B)** Comparison between the results obtained with the magnetometer (MinIMU9 v3, LMS303D) and the celestial compass to determine the robot's orientation. Weather conditions: clear sky, UV-index from 7 to 9. Adapted from [52]. **C** Heading angle errors in degrees, depending on the weather conditions: clear sky (left), variable sky (middle) and completely covered sky (right). From left to right, the median heading angle error was equal to 0.4°, −2.9°, and −1.9°, with no statistical difference between each other (Wilcoxon rank sum test, $P > 0.025$ using the Bonferronni correction); *NS:* non-significant. UV index was between 1 and 2 (source: French Meteorological services). Adapted from [51]. **D** Evolution of the heading angle ψ provided by the robot's magnetometer before (in red) and after (in blue) angular correction. These corrections were made using only the UV-polarized light compass during a straight forward walking task. Walking step measurements from 1 to 6 were acquired on 02/18/2017 while the next six measurements were acquired on 02/20/2017. Adapted from [51].

02/20/2017 under outdoor conditions, at any time of the day, in an open-air car park on the Luminy campus (43°14′01.6″N ; 5°26′39.2″E) of Aix Marseille Université, Marseille, France., The locomotor pattern of the Hexabot robotic platform used here was configured so as to produce tripod gait in all the navigational tasks tested. The angular resolution of the UV-polarized light compass was arbitrarily set at 1.29° with an acquisition time of 42 seconds.

5.1. Recovery of orientation under various weather conditions

The ability of the compass to reorientate Hexabot after undergoing a random yaw disturbance was first tested. The following reorientation tasks were performed for this purpose: (a) the robot recorded its initial heading angle with the celestial compass; (b) the robot turned by a random angle and then acquired the new heading angle; (c) the robot computed the difference between the initial and new heading angles and used this information to recover its initial orientation. Lastly, we compared the ground truth measurements (magnetometer[4]) before the disturbance and after the angular correction. The random heading angle shifts were set between −70° and +70°. An example of the re-orientation experiments performed under variable sky conditions is presented in Fig. 10. Fig. 9C shows the heading errors which occurred under the three different

[4]Experiments were conducted with a calibrated magnetometer, far from any magnetic field interferences.

weather conditions. The variability of the performances in terms of orientation recovery can be explained by the irregularity of Hexabot's stride length while turning due to interactions with the ground (see Fig. 2(Top) for details of the ground texture). Taking this point into account, these results correspond to excellent performances, especially under clear sky conditions. The increase in the mean error observed under both cloudy and overcast skies was due to the low degree of polarization of the skylight [22], which means that the Rayleigh scattering disturbed the pattern of polarization of the skylight. In comparison with the results obtained with the Sahabot robot in [28] (where the average angular error under mild weather conditions ranged from 1.73° to 0.66°, depending on the model), our UV-polarized light compass gave slightly better results under a clear sky (up to 54% improvement), and promising results under poor meteorological conditions such as a cloudy sky and a much lower level of UV radiance due to the time of year and the place where the experiments were performed. We applied the Wilcoxon rank sum test to investigate on whether the median errors between each weather conditions were different or not. Results showed that none of the median errors were different (clear vs. changeable: $P = 0.533$; clear vs. overcast: $P = 0.231$; changeable vs. overcast: $P = 0.928$), thus confirming the advantage of using the celestial compass in outdoor orientation.

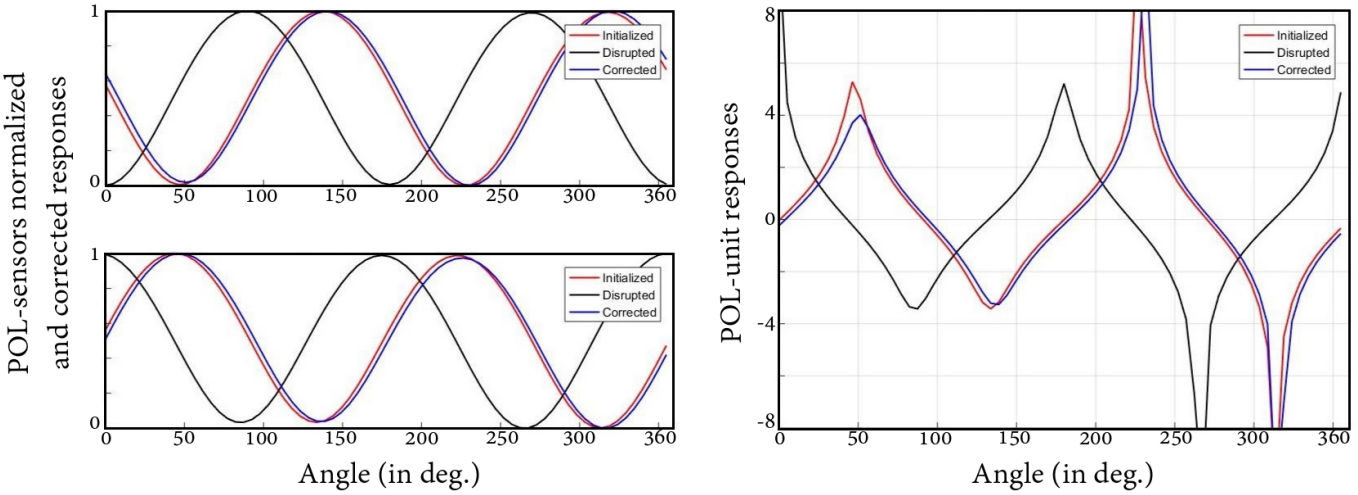

Figure 10: Example of results obtained during experiments in which Hexabot had to recover its initial heading angle after being randomly rotated. This test was performed under variable sky conditions with a low UV-index (approximately 1.2). Graphs on the left give the normalized and corrected signals UV_0^{nc} and UV_1^{nc} before (red) and after (black) the random turn, and after the heading angle recovery (blue). The corresponding POL-unit $p-$functions are given in the graph on the right. The robot's orientation recovery resulted in an error equal to 1.4°.

5.2. Heading-lock during a straight-forward walking task

Hexabot's performances showed the occurrence of large drifts on the yaw axis and the celestial compass corrected these yaw disturbances successfully. We then tested the ability of the compass to keep the robot on a straight forward trajectory, i.e. with a constant heading angle, by applying a one-shot yaw correction after each walking step. First the initial orientation was acquired. Hexabot then performed a series of strides for two seconds and measured its new heading angle, the value of which was compared with the initial one in order to compute the appropriate yaw correction to be applied. Lastly, Hexabot performed the corresponding turning movement before moving on to the next series of strides. Due to power supply limitations and so as to avoid the impact of any polarization shifts induced by the Sun's movements, data were acquired on two separate days (02/18/2017 and 02/20/2017), but the experiments were all performed at the same time of day (2:00 pm) under perfectly clear sky conditions (UV-index = 2). Results of all these experiments are shown in Fig. 9D. The mean heading angle error measured was $-0.3°$, which is consistent with the performances previously recorded under clear sky conditions. The peak error measured was 7.7° during the ninth walking step. Since there were no clouds in the sky at

that time, the pattern of polarization was fairly constant throughout the experiments. The heading angle errors were therefore mainly caused by interactions between the robot's legs and the ground.

The experiments performed here with Hexabot clearly show that our celestial compass is capable of making precise, reliable heading angle estimates under weather conditions of all kinds, regardless of the UV-index. However, Hexabot's turning movements are highly unpredictable and may affect the long-term navigation performances. A more stable hexapod robot is now required to ensure successful homing navigation.

6. Toward navigation skills: the odometric cues

Desert ants *Cataglyphis* are capable of integrating the distance travelled on the basis of their stride length and ventral OF integration processes [14, 17]. As experimental studies have shown that desert ants can use either of these sensory modes, it was proposed here to test all the possibilities involving these cues. The optic flow has long been used for odometric cues estimation [61, 62] as well as obstacle avoidance [63, 64, 65] or object tracking [66]. Multiple strategies have been proposed and mostly make use of high-resolution cameras[5]. In this study, AntBot is equipped with a 12-pixel OF sensor called M^{2}APix (Michaelis-Menten Auto-adaptive Pixels, Fig. 11A,D-E) which measures high rate OF with auto-adaptability to light changes within a 7-decade range [53].

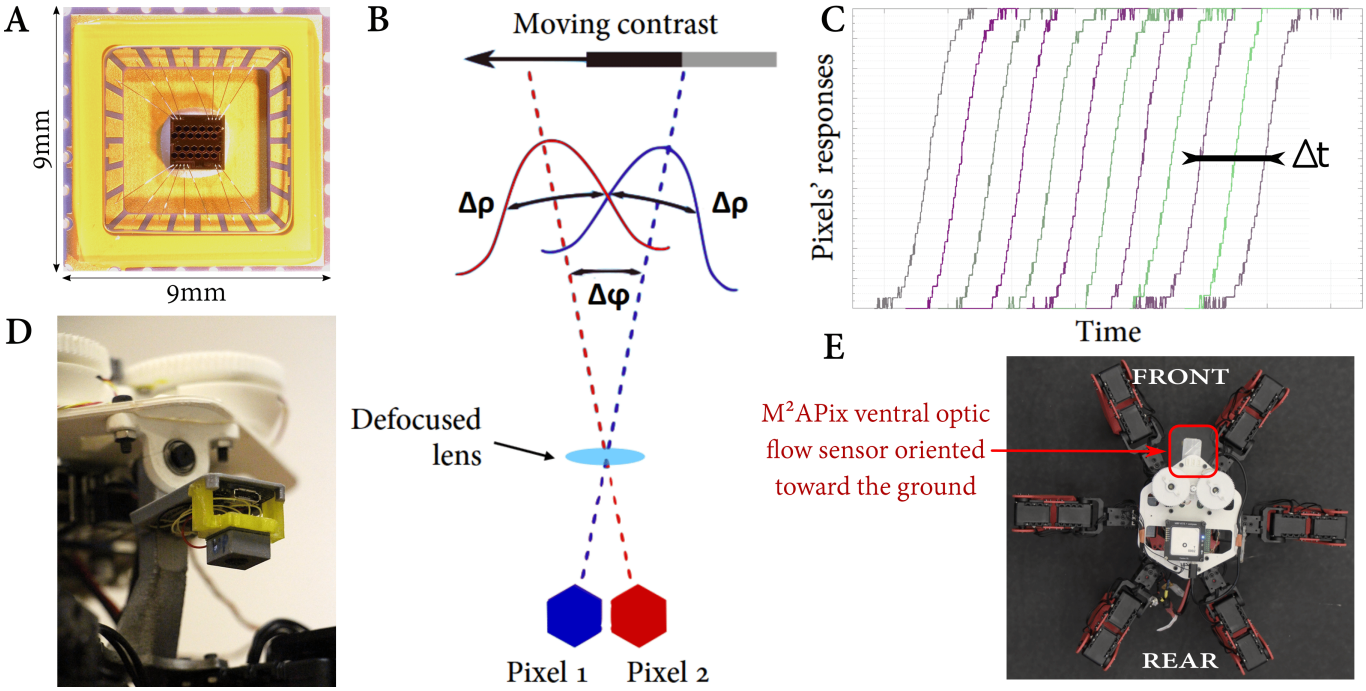

Figure 11: **(A)** The M^{2}APix silicon retina. Adapted from [53]. **(B)** Optical geometry explaining the visual signal acquisition depending on the inter-pixel angle $\Delta\varphi$ between two adjacent pixels (referred to as a local motion sensor LMS), and the acceptance angle $\Delta\rho$, defined as the width of the Gaussian angular sensitivity at half height. Adapted from [67]. **(C)** Raw signals obtained with the 12 pixels detecting a moving contrast. The first row of pixels gave the purple curves, while the second row of pixels gave the green curves. ΔT is the time elapsing between two adjacent pixels in a row. **(D)** Photograph of the M^{2}APix sensor topped with the lens of a Raspberry Pi NoIR camera and connected to the Teensy 3.2 micro-controller. **(E)** Top view of AntBot equipped with the OF sensor.

The distance *Dist* estimated after stride integration was defined as:

$$Dist = Stride \cdot d_{Stride} \tag{6}$$

where *Stride* is the number of strides performed and d_{Stride} is the average stride length. The other two methods implemented in this study involved the use of ventral OF. The ventral OF ω

[5]For a review on the most widespread techniques, please go to: http://www.scholarpedia.org/article/Optic_flow

(in rad/s) is given by (7), where $\Delta\varphi$ is the inter-pixel angle between two adjacent pixels in a row (Fig. 11B), ΔT is the mean time lag measured between two adjacent pixels' detection of the same moving contrast (Fig. 11C), $\mathcal{V}$ is the robot's ground speed, and D is the height of the OF sensor, which is assumed to be constant.

$$\omega = \frac{\Delta\varphi}{\Delta T} = \frac{\mathcal{V}}{D} \tag{7}$$

Based on the characterization of the M^{2}APix sensor described in [54], $\Delta\varphi = 3.57^\circ$ with a standard deviation of 0.027°. The time lag ΔT is then computed with the cross-correlation method described in [67], which is particularly suitable for performing low OF measurements. The OF-based distance is given by:

$$Dist = \frac{D \cdot \Delta\varphi \cdot T_{Stride}}{\Delta T} \tag{8}$$

where T_{Stride} is the duration of the walking phase. A third method of calculating the distance travelled consisted of taking the mean value between the stride length and the OF based distances, namely:

$$Dist = \frac{1}{2}\left(Stride \cdot d_{Stride} + \beta \cdot \frac{D \cdot \Delta\varphi \cdot T_{Stride}}{\Delta T} \right) \tag{9}$$

The β constant was set to adjust the OF calculations to the experimental conditions. The dynamic behavior of the Dynamixel servomotors AX18 of the AntBot robot depended on the ambient temperature, resulting in significant stride length variability, whether the experiments were performed in the morning (below 5°C) or the afternoon (above 10°C). In addition, the first and last strides caused unduly high OF as the robot's speed shifted from null to maximum (first stride), and from maximum to null (last stride). Shorter distances travelled therefore give less reliable OF values. A set of constants is given in Table 6.

Number of strides	β_M	β_A
1 or 2	0.667	0.500
3	0.850	0.750
More than 3	0.980	0.980

Table 6: Empirical gain β used for the outdoor experiments. β_M stands for the morning value of β, and β_A stands for the afternoon value.

7. Homing like desert ants

AntBot was built to meet the requirements of successful long-range navigation by decreasing the instability of the leg transfer phase and making the gait more robust. AntBot was designed to mimic ant-based tripod gait [68, 69]. The interactions between the legs and the ground were minimized using flat textured panels providing a good contrast to facilitate the ventral OF measurements. The celestial cue acquisition process was also improved. The acquisition time is now less than 20 seconds with an angular precision set at 0.96°.

The experiments were conducted both outdoors (using the celestial cues) and indoors (in the case of orientation-blind navigation modes). Indoor ground truth data were recorded by our motion capture system in the Flying Arena of the Mediterranean. Outdoor experiments were accompanied by photograph-based ground truth records. Photos were taken each time the robot stopped and were then post-processed to determine the robot's 2-D location. Post-processing was performed as follows: the perspective of the image was first corrected[6]; the location of the robot

[6]The free software used is available at: https://sourceforge.net/projects/perspectiveimg/

throughout the trajectory was then determined using a simple point-and-click program available in Matlab. PI in desert ants is based on both visual cues (the polarized pattern of the skylight and the ventral OF) and internal (stride integration) cues, which are used to compute the homing vector pointing toward the nest [7, 70]. Three different PI modes were implemented here in AntBot: (a) the first mode, which was called the blind PI mode, relied on stride integration alone to compute both the orientation and the distance of the homing vector on the basis of statistical knowledge about the average stride length (8.2cm per walking stride as shown in (6)) and the turning stride angle, given that the AntBot robot has an angular resolution $\delta\Psi = 10.9^\circ$ and thus yielding the following heading estimation:

$$\Psi = TurningStrides \cdot \delta\Psi \tag{10}$$

(b) the second method was again blind in terms of the orientation, as the robot still computed its heading angle after the turning stride integration, but the distance travelled was computed here by taking the mean walking stride length and the ventral OF integration; (c) the last PI mode tested was a completely ant-inspired mode: the distance was computed in the same way as in the previous model, but the heading angle was obtained via the celestial compass, as shown by the following equation:

$$\Psi = \frac{1}{4}\left(\underset{x\in[0;180]^\circ}{\arg\min}\, p(x) + \underset{x\in[0;180]^\circ}{\arg\max}\, p(x) + \underset{x\in[180;360]^\circ}{\arg\min}\; p(x) + \underset{x\in[180;360]^\circ}{\arg\max}\; p(x) - 180^\circ \right) \tag{11}$$

In these experiments, the computation of Ψ takes every peak in the log-ratio p into account, thus increasing the accuracy of the heading angle estimates.

7.1. Homing after a displacement

The robot's heading angle with respect to its initial heading is denoted by Ψ_{ROBOT} (12), while the heading angle relative to the solar azimuth computed by the celestial compass is given by Ψ. We take Ψ_{INIT} to denote the initial orientation given by the celestial compass. All the angular values are given in degrees.

$$\Psi_{ROBOT} = \Psi - \Psi_{INIT} \tag{12}$$

In each experiment, the robot was first placed at the starting point $(0,0)$. The operator then moved the robot to a random location $R = (x_r, y_r)$, the coordinates of which were transmitted to AntBot by the operator. In the PI modes (a) and (b) mentioned above, the robot's heading was determined by turning-stride integration. AntBot was therefore provided with its heading angle (determined by our motion capture system) both at the initialization and at the release point. The robot computed its homing vector, namely its homing distance $Dist_{HOMING}$ and its homing orientation Ψ_{HOMING} as follows:

$$Dist_{HOMING} = \sqrt{x_r^2 + y_r^2} \tag{13}$$

$$\Psi_{HOMING} = \begin{cases} atan\left(\frac{y_r}{x_r}\right), & \text{if } x_r < 0 \\ 180 + atan\left(\frac{y_r}{x_r}\right), & \text{if } x_r > 0 \end{cases} \tag{14}$$

If $x_r = 0.00$ with float precision, then $\Psi_{HOMING} = 0^\circ$ modulo 180°. The ambiguity is solved here using the turning stride integrator. To go back home, the robot splits its homing trajectory into a series of $N = 8$ regularly spaced checkpoints. At each checkpoint, its homing trajectory is reassessed in view of the current heading angle and the distance covered. The heading angle is computed in line with (10) or (11), and the distance travelled is computed using (6), (8) or (9), depending on the PI mode applied. The homing procedure has been completed once the robot

judges its distance to the goal to amount to less than one stride length (8.2cm). The navigation task is summed up in algorithm 2.

Algorithm 2 The navigation experiment procedure: homing after being displaced. $Stride[i]$ is the number of strides to be walked until the next stop. T_h is the turning order required to make the robot correctly oriented toward its home location. $N = 8$ is the number of trajectory sections to be performed during the inbound phase. These sections involve strides of of two kinds: turning strides and straight forward ones. $\delta\Psi = 10.9^\circ$ is the angular resolution of AntBot.

AntBot is at location $(0,0)$ and orientation Ψ_{init} is acquired
AntBot is moved to $C_0 = (X_0, Y_0)$ and orientation Ψ_0 is acquired
Computation of $DIST_{HOMING}$, Ψ_{HOMING}, $Stride[i]_{i\in[1..N]}$ and T_h
AntBot rotates by T_h
$i = 1$
while $i \leq N$ **do**
    Walk for $Stride[i]$ strides
    Update the location $C_i = (X_i, Y_i)$
    Computation of the new optimum $DIST_{HOMING}$ and Ψ_{HOMING}
    if $i < N$ **then**
        Update the remaining series of strides $Stride[i]_{i\in[i+1..N]}$
    end
    if $|\Psi_{HOMING} - \Psi_{ROBOT}| > \delta\Psi$ **then**
        Update the turning order T_h
        AntBot rotates for T_h strides
    end
    $i = i + 1$
end

The three PI methods were tested five times each during late February 2018 at the same place as the experiments performed with Hexabot. The blind method gave poor results, including a mean error of 124cm $\pm$ 59cm (mean $\pm$ standard deviation), while the half-blind method (distance: ventral OF and stride integration; heading: stride integration) gave an almost twice lower mean error and the same standard deviation (74cm $\pm$ 62cm). The results obtained with the full sensor PI method are presented in Fig. 12. With this method, AntBot reached the homing point with a mean error of only 4.8cm $\pm$ 1.9cm. This latter error was statistically lower than the two others as shown through the Wilcoxon signed-rank test ($P > 0.025$ using the Bonferonni correction).

7.2. Autonomous navigation

To confirm the trends shown by the results obtained in the first few experiments, we conducted a further series of five full homing tests with the 3 different PI approaches mentioned above (with a clear sky, UV-index ≈ 1.8). In these experiments, the robot was made to perform a predetermined outbound trajectory including five checkpoints $C_i = (x_i, y_i), i \in [\![1..5]\!]$. Once AntBot had reached the last checkpoint, it computed its homing vector on the basis of the navigation cues acquired during the whole trajectory (15) depending on which of the three PI methods was tested. A geometrical view of the 5-checkpoint homing trajectory is shown in Fig. 13.

$$\begin{cases} x_i = x_{i-1} + Dist_i * \cos\left(\Psi_{ROBOT,i}\right) \\ y_i = y_{i-1} + Dist_i * \sin\left(\Psi_{ROBOT,i}\right) \end{cases} \tag{15}$$

Lastly, the homing distance and the heading were computed using (13) and (14), respectively, switching from (x_r, y_r) to (x_5, y_5). The navigation routine is summarized in algorithm 3. These experiments were conducted between late February and early March 2018 at the same place as all the previous experiments, under a clear sky (with a UV-index ranging from 2 to 2.8). The overall 2-D trajectories are shown in fig. 14.

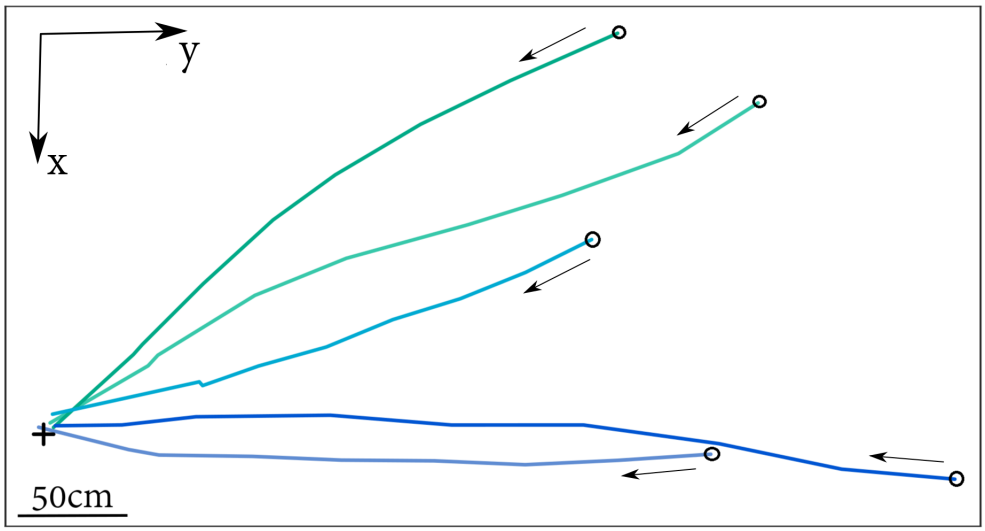

Figure 12: Homing trajectories recorded with the full sensor method (distance: ventral OF and stride integration; heading: celestial compass). Black circles give the release point and the black cross gives the homing point.

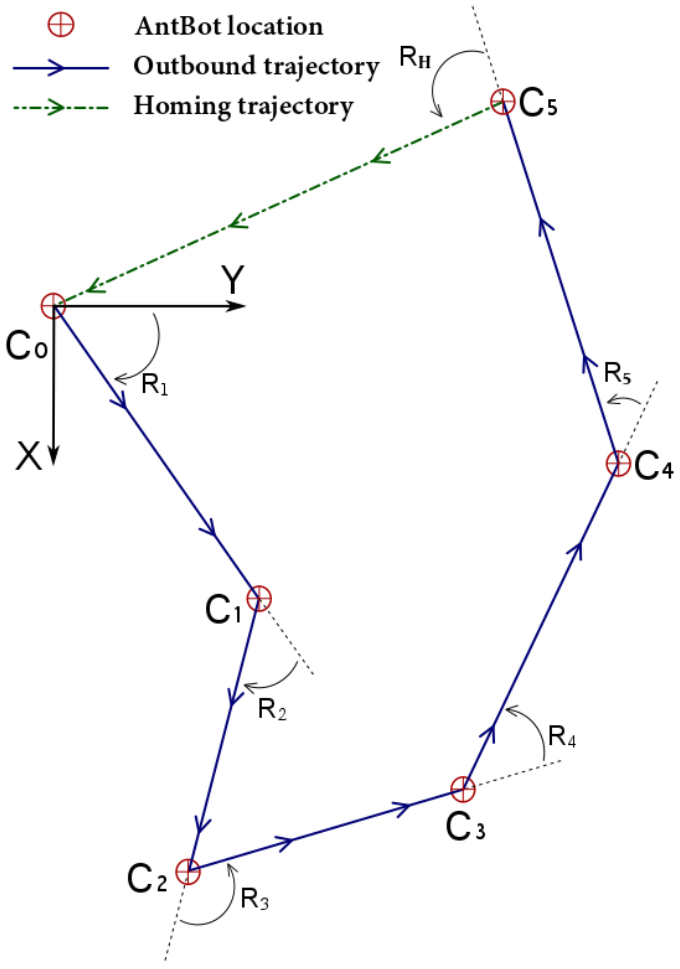

Figure 13: Theoretical homing trajectory (green) after an outbound trajectory including 5 checkpoints C_1 to C_5 (blue). R_i denotes the rotation performed by AntBot between one heading angle and the next, and R_H denotes the homing turning angle.

The overall results obtained are given in Table 7 and compared with those obtained by Lambrinos with Sahabot 2 in [29]. The entirely blind PI method resulted in large homing errors due to the great variability of the angular values and the stride lengths. As the robot was not informed about its drift, errors occurred along the whole trajectory. Adding the OF component significantly improved the results: the AntBot's final locations were closer to the average final location, which

Algorithm 3 The navigation experiment procedure: fully autonomous navigation. $Stride[i]$ is the number of strides to be walked until the next stop. T_h is the turning order making the robot correctly oriented toward its home location. $N_{OUTBOUND} = 5$ is the number of trajectory sections to be performed during the outbound phase. The strides in these sections are of two kinds: turning strides and straight-forward ones. $N_{INBOUND} = 8$ is the number of trajectory sections performed during the homing phase. $\delta\Psi = 10.9^\circ$ is AntBot's angular resolution.

AntBot is at location $(0,0)$ and orientation Ψ_{init} is acquired
$i = 1$
while $i \leq N_{OUTBOUND}$ **do**
    Turn for $T_h[i]$ strides
    Walk for $Stride[i]$ strides
    Acquire new orientation Ψ_i
    Update the location $C_i = (X_i, Y_i)$
    $i = i + 1$
end
Computation of $DIST_{HOMING}$, Ψ_{HOMING}, $Stride[i]_{i\in[1..N]}$ and T_h
AntBot rotates for T_h strides
$i = 1$
while $i \leq N_{INBOUND}$ **do**
    Walk for $Stride[i]$ strides
    Update the location $C_i = (X_i, Y_i)$
    Computation of the new optimal $DIST_{HOMING}$ and Ψ_{HOMING}
    if $i < N_{INBOUND}$ **then**
        Update the remaining series of strides $Stride[i]_{i\in[i+1..N_{INBOUND}]}$
    end
    if $|\Psi_{HOMING} - \Psi_{ROBOT}| > \delta\Psi$ **then**
        Update the turning order T_h
        AntBot rotates for T_h strides
    end
    $i = i + 1$
end

was not the case with the blind method (see Fig. 14 A and B). Yet the mean error was still too large to be able to say that the homing was successful. Lastly, the fully ant-inspired method gave better results with a mean homing error of 5.0cm. As the AntBot is 450mm wide, this error corresponds to 11% of the robot's size, and this error is below the minimum stride length the AntBot can produce. This entirely bio-inspired homing method can therefore be said to be highly successful.

8. Summary and conclusion

In this study, two autonomous hexapod robots (Hexabot and AntBot) were used to investigate several desert ant-inspired path integration (PI) methods. The robots were equipped with two minimalistic sensors inspired by these insects' compound eye: a 2-pixel celestial compass endowed with spectral sensitivity in the ultraviolet (UV) range, equivalent to two arrays of 374 pixels, and a 12-pixel auto-adaptive optic flow (OF) sensor. In desert ants, the PI process is based on a homing vector that always points toward the nest. The heading angle is determined on the basis of celestial cues consisting of the linear polarization of the skylight in the UV range, as well as the position of the sun in the sky dome and the color gradient across the sky. These cues are detected via the dorsal rim area (DRA) of the insects' compound eye. The desert ants' odometer is known to function using both stride-counting and ventral OF cues. These navigation cues make them go straight back to their nest, giving outstanding homing performances. Except for the color

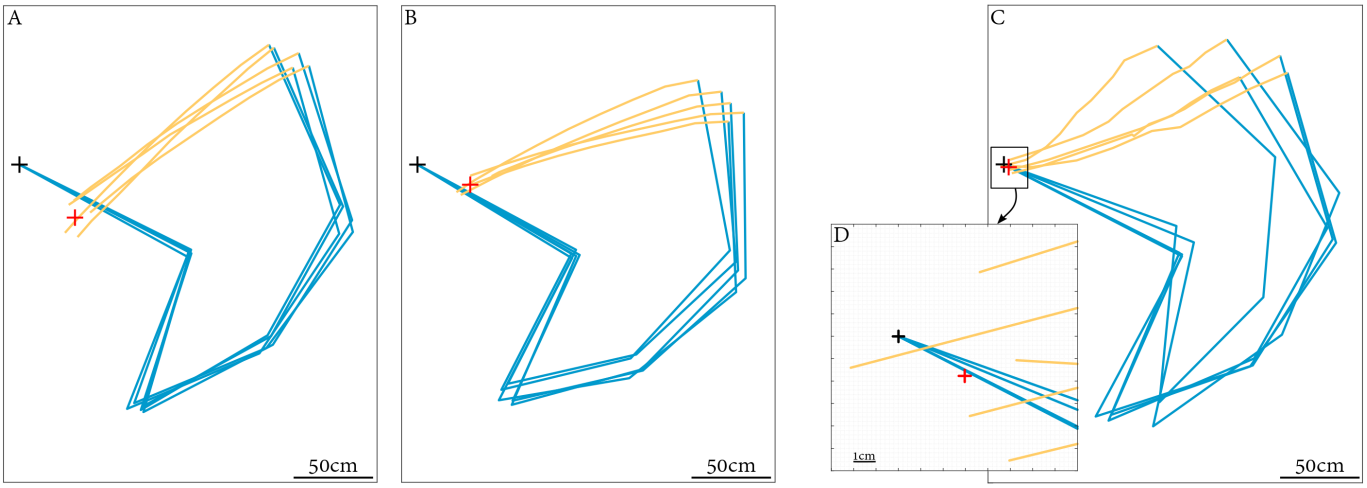

Figure 14: Navigation results obtained with **A** the blind method (stride-based estimates of the orientation and the distance), **B** the half-blind method (stride-based estimates of the orientation, and the distance is estimated using both the ventral OF and the stride integration), and **C** the full sensor method (celestial-based orientation and both ventral OF and stride based distance estimates). **D** Magnified view of the homing performances of the full sensor method shown in (C). In all the graphs, the black cross gives the starting point at (0,0), and the red cross gives the average homing position reached. Outbound trajectories are presented in blue, and homing trajectories in yellow. The variability in the outbound trajectories in (C) is due to the varying outdoor temperatures (below 5°C in the morning, and above 10°C in the afternoon) which had considerable effects on the dynamics of the servomotors. The same outbound trajectory was used in all the experiments (both indoors and outdoors). The orders consisted in the number of walking and turning strides to be performed between two successive checkpoints.

gradient, these sensory processing modes have all been mimicked on-board AntBot.

The celestial compass embedded on board our hexapod robots has been closely studied and characterized. It gives precise, robust estimates of the robot's heading angle under a clear sky regardless of the UV-index. The median angular errors obtained under both variable and covered skies suggest that this sensor can be used under all these conditions, again regardless of the UV-index. In addition, it was found to be highly resilient to the occlusion of its field of view by tree canopies. Underwater tests also brought to light some other interesting characteristics, especially when water droplets were placed on top of the sensor. Preliminary tests on the celestial compass fully immersed in freshwater had to be conducted in order to determine whether it is suitable for use in marine environments. Prior applications of the celestial compass were tested with Hexabot. Open-loop corrections to the robot's movements on the yaw axis led to small angular errors, most of which can be explained by the interactions between the legs and the ground.

The PI was then tested with AntBot, in which the heading and the distance travelled were merged into a homing vector pointing toward the nest entrance. Three models were tested for this purpose: the blind PI, the half-blind PI, and the fully ant-inspired PI. The blind and half-blind PI modes yielded heading estimations based on turning stride integration. A numerical comparison with the performances of Lambrinos' Sahabot 2 [29] is made in Table 7. The blind PI gave the least satisfactory results with a mean homing error of 49.0cm $\pm$ 8.12cm. Introducing OF measurements into the half-blind PI mode to improve the distance estimates reduced the mean homing error by only 13cm, whereas adding celestial cues to the third PI mode considerably improved the accuracy of the navigation performances, resulting in a mean homing error of only 5.0cm $\pm$ 1.8cm. These results show that the estimation of the heading is a critical parameter in PI-based navigation, which is completely in line with recent findings on desert ants whose PI processes are mainly based on the pattern of polarization of the skylight [71, 72].

The absolute homing error achieved by AntBot endowed with the full sensory PI mode was almost 3 times better than that of Sahabot 2. However, the trajectories studied here were only 7m long, whereas those taken by Sahabot 2 were up to 70m long. The mean error relative to the total length of the trajectory was therefore approximately 0.7% with AntBot, as compared with only 0.2% in the case of Sahabot 2. Several hypotheses can be put forward to explain this difference.

	Characteristics	Minimum	Maximum	Median	Mean	SD
Blind PI	Distance: strides (6)					
	Heading: strides (10)	40.1	58.5	51.7	49.0	8.12
Half-blind PI	Distance: strides + ventral OF (9)					
	Heading: strides (10)	30.1	47.3	33.9	36.3	6.6
Full sensor PI	Distance: strides + ventral OF (9)					
	Heading: POL-compass (11)	2.5	7.4	4.8	5.0	1.8
Sahabot 2	Distance: wheel encoders					
	Heading: POL-compass	5	27	-	13.5	6.3

Table 7: Overall homing errors (in cm) obtained here in all the homing experiments, and comparison with the results obtained by Lambrinos with Sahabot 2 in [29]. All the numerical values are given in centimeters. SD: standard deviation. AntBot's complete trajectory: 7m; Sahabot's complete trajectory: 70m.

First, AntBot is a legged robot, which makes it highly prone to drifting from its path. This drift was determined quantitatively with Hexabot (34cm after a 1m-straight-forward walk at 35cm/s). Since the two robots are both controlled with the same firmware, a similar range of drift can be expected to occur with AntBot. Another hypothesis might be that the odometric cues used by AntBot are coarser than in Sahabot. Stride-counting odometry is performed by simply multiplying the number of strides by the average stride length (8.2cm), the value of which depends on the dynamics of the servomotors which is known to depend in turn on the temperature of the actuator, but the fatigue of the plastic gears also plays a role. OF measurements are also prone to errors because of the irregular pattern of the walking speed: the speed is linear in wheeled robots, whereas legged robots show hectic variations in the acceleration whether or not the leg is in the transfer phase [50]. It would be worth investigating in the future whether or not the length of the trajectory affects the AntBot's homing performances. The fully ant-inspired PI mode gave the same homing errors in the two navigational experiments performed in this study. This suggests that this PI mode may be less prone to cumulative errors than the other ones tested. This finding will have to be confirmed in further experiments including outbound trajectories with various shapes and distances. At last, the relative mean homing error of 0.7% performed with AntBot is currently rather good in comparison with the current state-of-the-art in visual odometry, such as the 1.3% relative precision of a sky compass-based egomotion estimation system [73].

The different ways in which celestial cues are acquired could also be one of the reasons why the relative error was lower in the case of Sahabot 2 than AntBot. However, the Sahabot model for polarization-based heading estimation has been compared to the AntBot model in a recent study under three distinct weather conditions: under a clear, changeable and overcast sky [35]. The Sahabot model gave the least satisfactory results under all the weather conditions tested, which differed significantly from those obtained with our AntBot method. Our celestial compass consists of only 2 pixels, but the rotation of the filters makes this number equivalent to two arrays of 374 pixels, i.e. 374 POL-units (time multiplexing), while Sahabot relies on only 3 POL-units to estimate its heading. It has been reported that the sine waves acquired with a POL-unit are very noisy due to the composition of the atmosphere [51]. Therefore, there is a higher risk of misestimating the AoP if only 3 POL-units are taken into account. Besides increasing the accuracy of the AoP estimates, our time-multiplexing solution considerably reduces the production cost of the sensor while mimicking the sensitivity of the ommatidia in the DRA of the desert ant's compound eye. The celestial compasses embedded on-board Sahabot 2 and AntBot were both inspired by the polarization-opponent model initially proposed by T. Labhart in crickets [19], and the polarization pathway outlined in [24, 25]. The main difference depends on where the information is taken: in AntBot, the heading is determined directly, based on the output of the POL-units in the DRA-like compass; in Sahabot, only three orientations (0°, 60° and 120°) are taken into account, thus mimicking the second stage in the polarization pathway processing which occurs in the insects' optic lobe. Comparisons between the two methods raise questions about the continuity of

the polarization pathway: why may it be advantageous to extract the AoP in the central complex based on the three orientations for which neurons in the optic lobe are specific (10°, 60° and 130°)?

These robotic applications of biological models for desert ants' navigation processes yield interesting field results which help to show how biologically plausible these models are. The AntBot robot is the first ant-like robot equipped with ant-inspired sensors and ant-based PI systems. It has accomplished astounding performances, reaching a homing error of only 0.7% with as few as 14 pixels. AntBot is therefore an excellent example of the advantages of the biorobotic approach presented in in [74, 75, 20, 63]: this fully open-source autonomous robot uses bio-inspired solutions which can take over from traditional methods (such as GPS and IMUs) in the event of their failure. Among the advantages of these methods is their low computational cost and the fact that they provide biologists with valuable feedback which can be used to refine their biological models. Some of the next steps will be to embed a panoramic visual sensor on-board the AntBot robot to mimick the ants' visual system with a coarse resolution of $5^\circ - 10^\circ$ [76] to both improve the robot's navigation performance and to assess obstacle avoidance skills.

Acknowledgements

The authors would like to thank Marc Boyron and Julien Diperi for their technical assistance with designing the celestial compass, and Jessica Blanc for revising the English manuscript.

Funding

This research was supported by the French Direction Générale de l'Armement (DGA), CNRS, Aix Marseille Université, the Provence-Alpes-Côte d'Azur region, and the French National Research Agency for Research (ANR) with the Equipex/Robotex project.

References

[1] E. Bergamini, G. Ligorio, A. Summa, G. Vannozzi, A. Cappozzo, A. M. Sabatini, Estimating orientation using magnetic and inertial sensors and different sensor fusion approaches: Accuracy assessment in manual and locomotion tasks, Sensors 14 (10) (2014) 18625–18649. doi:10.3390/s141018625.

[2] R. Wehner, B. Michel, P. Antonsen, Visual navigation in insects: coupling of egocentric and geocentric information, Journal of Experimental Biology 199 (1) (1996) 129–140.

[3] T. Labhart, E. P. Meyer, Neural mechanisms in insect navigation: polarization compass and odometer, Current opinion in neurobiology 12 (6) (2002) 707–714. doi:10.1016/S0959-4388(02)00384-7.

[4] K. Coulson, Characteristics of the radiation emerging from the top of a rayleigh atmospherei: Intensity and polarization, Planetary and Space Science 1 (4) (1959) 265–276. doi:10.1016/0032-0633(59)90031-5.

[5] K. Coulson, Polarization and Intensity of Light in the Atmosphere, A Deepak Pub, 1988.

[6] R. Wehner, The desert ant's navigational toolkit: procedural rather than positional knowledge, Navigation 55 (2) (2008) 101–114. doi:10.1002/j.2161-4296.2008.tb00421.x.

[7] M. Müller, R. Wehner, Path integration in desert ants, cataglyphis fortis, Proceedings of the National Academy of Sciences 85 (14) (1988) 5287–5290. doi:10.1073/pnas.85.14.5287.

[8] R. Wehner, Desert ant navigation: how miniature brains solve complex tasks, Journal of Comparative Physiology A 189 (8) (2003) 579–588. doi:10.1007/s00359-003-0431-1.

[9] M. Knaden, R. Wehner, Path integration in desert ants controls aggressiveness, Science 305 (5680) (2004) 60–60. doi:10.1126/science.1097165.

[10] R. Wehner, S. Wehner, Insect navigation: use of maps or ariadne's thread?, Ethology Ecology & Evolution 2 (1) (1990) 27–48. doi:10.1080/08927014.1990.9525492.

[11] M. V. Srinivasan, Going with the flow: a brief history of the study of the honeybees navigational odometer, Journal of Comparative Physiology A 200 (6) (2014) 563–573. doi:10.1007/s00359-014-0902-6.

[12] B. Cartwright, T. S. Collett, Landmark learning in bees, Journal of comparative physiology 151 (4) (1983) 521–543. doi:10.1007/BF00605469.

[13] B. Cartwright, T. Collett, Landmark maps for honeybees, Biological cybernetics 57 (1-2) (1987) 85–93. doi:10.1007/BF00318718.

[14] B. Ronacher, R. Wehner, Desert ants cataglyphis fortis use self-induced optic flow to measure distances travelled, Journal of Comparative Physiology A 177 (1) (1995) 21–27. doi:10.1007/BF00243395.

[15] J. Zeil, M. I. Hofmann, J. S. Chahl, Catchment areas of panoramic snapshots in outdoor scenes, JOSA A 20 (3) (2003) 450–469. doi:10.1364/JOSAA.20.000450.

[16] A. Wystrach, S. Schwarz, P. Schultheiss, G. Beugnon, K. Cheng, Views, landmarks, and routes: how do desert ants negotiate an obstacle course?, Journal of Comparative Physiology A 197 (2) (2011) 167–179. doi:10.1007/s00359-010-0597-2.

[17] M. Knaden, P. Graham, The sensory ecology of ant navigation: from natural environments to neural mechanisms, Annual review of entomology 61 (2016) 63–76. doi:10.1146/annurev-ento-010715-023703.

[18] T. Labhart, E. P. Meyer, Detectors for polarized skylight in insects: a survey of ommatidial specializations in the dorsal rim area of the compound eye, Microscopy research and technique 47 (6) (1999) 368–379. doi:10.1002/(SICI)1097-0029(19991215)47:6<368::AID-JEMT2>3.0.CO;2-Q.

[19] T. Labhart, Polarization-opponent interneurons in the insect visual system, Nature 331 (6155) (1988) 435. doi:10.1038/331435a0.

[20] M. V. Srinivasan, Honeybees as a model for the study of visually guided flight, navigation, and biologically inspired robotics, Physiological reviews 91 (2) (2011) 413–460. doi:10.1152/physrev.00005.2010.

[21] G. Horváth, D. Varjú, Polarized light in animal vision: polarization patterns in nature, Springer Science & Business Media, 2013.

[22] M. L. Brines, J. L. Gould, Skylight polarization patterns and animal orientation, Journal of Experimental Biology 96 (1) (1982) 69–91.

[23] A. Barta, G. Horváth, Why is it advantageous for animals to detect celestial polarization in the ultraviolet? skylight polarization under clouds and canopies is strongest in the uv, Journal of Theoretical Biology 226 (4) (2004) 429–437. doi:10.1016/j.jtbi.2003.09.017.

[24] U. Homberg, In search of the sky compass in the insect brain, Naturwissenschaften 91 (5) (2004) 199–208. doi:10.1007/s00114-004-0525-9.

[25] M. Sakura, D. Lambrinos, T. Labhart, Polarized skylight navigation in insects: model and electrophysiology of e-vector coding by neurons in the central complex, Journal of neurophysiology 99 (2) (2008) 667–682. doi:10.1152/jn.00784.2007.

[26] S. Heinze, U. Homberg, Linking the input to the output: new sets of neurons complement the polarization vision network in the locust central complex, Journal of Neuroscience 29 (15) (2009) 4911–4921. doi:10.1523/JNEUROSCI.0332-09.2009.

[27] A. Cheung, Animal path integration: a model of positional uncertainty along tortuous paths, Journal of theoretical biology 341 (2014) 17–33. doi:10.1016/j.jtbi.2013.09.031.

[28] D. Lambrinos, H. Kobayashi, R. Pfeifer, M. Maris, T. Labhart, R. Wehner, An autonomous agent navigating with a polarized light compass, Adaptive behavior 6 (1) (1997) 131–161. doi:10.1177/105971239700600104.

[29] D. Lambrinos, R. Möller, T. Labhart, R. Pfeifer, R. Wehner, A mobile robot employing insect strategies for navigation, Robotics and Autonomous systems 30 (1-2) (2000) 39–64. doi:10.1016/S0921-8890(99)00064-0.

[30] M. Bech, U. Homberg, K. Pfeiffer, Receptive fields of locust brain neurons are matched to polarization patterns of the sky, Current Biology 24 (18) (2014) 2124–2129. doi:10.1016/j.cub.2014.07.045.

[31] J. Chu, K. Zhao, Q. Zhang, T. Wang, Construction and performance test of a novel polarization sensor for navigation, Sensors and Actuators A: Physical 148 (1) (2008) 75–82. doi:10.1016/j.sna.2008.07.016.

[32] J. Chahl, A. Mizutani, Biomimetic attitude and orientation sensors, IEEE Sensors Journal 12 (2) (2012) 289–297. doi:10.1109/JSEN.2010.2078806.

[33] Y. Wang, J. Chu, R. Zhang, L. Wang, Z. Wang, A novel autonomous real-time position method based on polarized light and geomagnetic field, Scientific reports 5 (2015) 9725. doi:10.1038/srep09725.

[34] W. Zhi, J. Chu, J. Li, Y. Wang, A novel attitude determination system aided by polarization sensor, Sensors 18 (1) (2018) 158. doi:10.3390/s18010158.

[35] J. Dupeyroux, S. Viollet, J. R. Serres, Polarized skylight-based heading measurements: a bio-inspired approach, Journal of The Royal Society Interface 16 (150) (2019) 20180878. doi:10.1098/rsif.2018.0878.

[36] M. Sarkar, D. S. S. Bello, C. Van Hoof, A. Theuwissen, Integrated polarization-analyzing cmos image sensor for detecting the incoming light ray direction, IEEE Transactions on Instrumentation and Measurement 60 (8) (2011) 2759–2767. doi:10.1109/TIM.2011.2130050.

[37] J. Chu, Z. Wang, L. Guan, Z. Liu, Y. Wang, R. Zhang, Integrated polarization dependent photodetector and its application for polarization navigation, IEEE Photonics Technol. Lett 26 (5) (2014) 469–472. doi:10.1109/LPT.2013.2296945.

[38] M. Garcia, C. Edmiston, R. Marinov, A. Vail, V. Gruev, Bio-inspired color-polarization imager for real-time in situ imaging, Optica 4 (10) (2017) 1263–1271. doi:10.1364/OPTICA.4.001263.

[39] N. Carey, W. Stürzl, An insect-inspired omnidirectional vision system including uv-sensitivity and polarisation, in: Computer Vision Workshops (ICCV Workshops), 2011 IEEE International Conference on, IEEE, 2011, pp. 312–319. doi:10.1109/ICCVW.2011.6130258.

[40] M. Sarkar, D. S. S. Bello, C. van Hoof, A. J. Theuwissen, Biologically inspired cmos image sensor for fast motion and polarization detection, IEEE Sensors Journal 13 (3) (2013) 1065–1073. doi:10.1109/JSEN.2012.2234101.

[41] D. Wang, H. Liang, H. Zhu, S. Zhang, A bionic camera-based polarization navigation sensor, Sensors 14 (7) (2014) 13006–13023. doi:10.3390/s140713006.

[42] W. Zhang, Y. Cao, X. Zhang, Z. Liu, Sky light polarization detection with linear polarizer triplet in light field camera inspired by insect vision, Applied optics 54 (30) (2015) 8962–8970. doi:10.1364/AO.54.008962.

[43] C. Fan, X. Hu, J. Lian, L. Zhang, X. He, Design and calibration of a novel camera-based bio-inspired polarization navigation sensor, IEEE Sensors Journal 16 (10) (2016) 3640–3648. doi:10.1109/JSEN.2016.2533628.

[44] W. Zhang, X. Zhang, Y. Cao, H. Liu, Z. Liu, Robust sky light polarization detection with an s-wave plate in a light field camera, Applied optics 55 (13) (2016) 3518–3525. doi:10.1364/AO.55.003518.

[45] Y. Wang, X. Hu, L. Zhang, J. Lian, X. He, Polarized light compass-aided visual-inertial navigation under foliage environment, IEEE Sensors Journal 17 (17) (2017) 5646–5653. doi:10.1109/JSEN.2017.2725938.

[46] G. Han, X. Hu, J. Lian, X. He, L. Zhang, Y. Wang, F. Dong, Design and calibration of a novel bio-inspired pixelated polarized light compass, Sensors 17 (11) (2017) 2623. doi:10.3390/s17112623.

[47] C. Fan, X. Hu, X. He, L. Zhang, J. Lian, Integrated polarized skylight sensor and mimu with a metric map for urban ground navigation, IEEE Sensors Journal 18 (4) (2018) 1714–1722. doi:10.1109/JSEN.2017.2786404.

[48] M. Momeni, A. H. Titus, An analog vlsi chip emulating polarization vision of octopus retina, IEEE transactions on neural networks 17 (1) (2006) 222–232. doi:10.1109/TNN.2005.860865.

[49] J. Chu, H. Wang, W. Chen, R. Li, Application of a novel polarization sensor to mobile robot navigation, in: Mechatronics and Automation, 2009. ICMA 2009. International Conference on, IEEE, 2009, pp. 3763–3768. doi:10.1109/ICMA.2009.5245970.

[50] J. Dupeyroux, G. Passault, F. Ruffier, S. Viollet, J. Serres, Hexabot: a small 3d-printed six-legged walking robot designed for desert ant-like navigation tasks, in: IFAC Word Congress 2017, 2017, pp. 1628–1631.

[51] J. Dupeyroux, J. Diperi, M. Boyron, S. Viollet, J. Serres, A bio-inspired celestial compass applied to an ant-inspired robot for autonomous navigation, in: ECMR-European Conference on Mobile Robotics, 2017, pp. 119–124. doi:10.1109/ECMR.2017.8098680.

[52] J. Dupeyroux, J. Diperi, M. Boyron, S. Viollet, J. Serres, A novel insect-inspired optical compass sensor for a hexapod walking robot, in: IROS 2017-IEEE/RSJ International Conference on Intelligent Robots and Systems, 2017, pp. 3439–3445. doi:10.1109/IROS.2017.8206183.

[53] S. Mafrica, S. Godiot, M. Menouni, M. Boyron, F. Expert, R. Juston, N. Marchand, F. Ruffier, S. Viollet, A bio-inspired analog silicon retina with michaelis-menten auto-adaptive pixels sensitive to small and large changes in light, Optics express 23 (5) (2015) 5614–5635. doi:10.1364/OE.23.005614.

[54] J. Dupeyroux, V. Boutin, J. R. Serres, L. U. Perrinet, S. Viollet, M^{2}apix: a bio-inspired auto-adaptive visual sensor for robust ground height estimation, in: 2018 IEEE International Symposium on Circuits and Systems (ISCAS), IEEE, 2018, pp. 1–4. doi:10.1109/ISCAS.2018.8351433.

[55] T. H. Waterman, Polarization patterns in submarine illumination, Science 120 (3127) (1954) 927–932. doi:10.2307/1682610.

[56] Y. Y. Schechner, N. Karpel, Clear underwater vision, in: Proceedings of the 2004 IEEE Computer Society Conference on Computer Vision and Pattern Recognition, 2004. CVPR 2004., Vol. 1, 2004, pp. I–I. doi:10.1109/CVPR.2004.1315078.

[57] T. H. Waterman, Reviving a neglected celestial underwater polarization compass for aquatic animals, Biological Reviews 81 (1) (2006) 111–115. doi:10.1017/S1464793105006883.

[58] A. Lerner, S. Sabbah, C. Erlick, N. Shashar, Navigation by light polarization in clear and turbid waters, Philosophical Transactions of the Royal Society B: Biological Sciences 366 (1565) (2011) 671–679. doi:10.1098/rstb.2010.0189.

[59] N. J. Marshall, A unique colour and polarization vision system in mantis shrimps, Nature 333 (6173) (1988) 557. doi:10.1038/333557a0.

[60] H. H. Thoen, M. J. How, T.-H. Chiou, J. Marshall, A different form of color vision in mantis shrimp, Science 343 (6169) (2014) 411–413. doi:10.1126/science.1245824.

[61] H. Dahmen, A. Millers, H. A. Mallot, Insect-inspired odometry by optic flow recorded with optical mouse chips, in: Flying insects and robots, Springer, 2009, pp. 115–126. doi:10.1007/978-3-540-89393-6_9.

[62] N. Nourani-Vatani, J. Roberts, M. V. Srinivasan, Practical visual odometry for car-like vehicles, in: 2009 IEEE International Conference on Robotics and Automation, IEEE, 2009, pp. 3551–3557. doi:10.1109/ROBOT.2009.5152403.

[63] N. Franceschini, Small brains, smart machines: from fly vision to robot vision and back again, Proceedings of the IEEE 102 (5) (2014) 751–781. doi:10.1109/JPROC.2014.2312916.

[64] K. McGuire, G. De Croon, C. De Wagter, K. Tuyls, H. Kappen, Efficient optical flow and stereo vision for velocity estimation and obstacle avoidance on an autonomous pocket drone, IEEE Robotics and Automation Letters 2 (2) (2017) 1070–1076. doi:10.1109/LRA.2017.2658940.

[65] T. A. Sarmiento, R. R. Murphy, Insights on obstacle avoidance for small unmanned aerial systems from a study of flying animal behavior, Robotics and Autonomous Systems 99 (2018) 17–29. doi:10.1016/j.robot.2017.09.002.

[66] F. Colonnier, S. Ramirez-Martinez, S. Viollet, F. Ruffier, A bio-inspired sighted robot chase like a hoverfly, Bioinspiration & biomimeticsdoi:10.1088/1748-3190/aaffa4.

[67] E. Vanhoutte, S. Mafrica, F. Ruffier, R. J. Bootsma, J. Serres, Time-of-travel methods for measuring optical flow on board a micro flying robot, Sensors 17 (3) (2017) 571. doi:10.3390/s17030571.

[68] C. Zollikofer, Stepping patterns in ants-influence of speed and curvature, Journal of experimental biology 192 (1) (1994) 95–106.

[69] C. Zollikofer, Stepping patterns in ants-influence of body morphology, Journal of experimental biology 192 (1) (1994) 107–118.

[70] A. Cheung, R. Vickerstaff, Finding the way with a noisy brain, PLoS computational biology 6 (11) (2010) e1000992. doi:10.1371/journal.pcbi.1000992.

[71] F. Lebhardt, J. Koch, B. Ronacher, The polarization compass dominates over idiothetic cues in path integration of desert ants, Journal of Experimental Biology 215 (3) (2012) 526–535. doi:10.1242/jeb.060475.

[72] F. Lebhardt, B. Ronacher, Interactions of the polarization and the sun compass in path integration of desert ants, Journal of Comparative Physiology A 200 (8) (2014) 711–720. doi:10.1007/s00359-013-0871-1.

[73] T. Jouir, R. Strydom, T. M. Stace, M. V. Srinivasan, Vision-only egomotion estimation in 6dof using a sky compass, Robotica 36 (10) (2018) 15711589. doi:10.1017/S0263574718000577.

[74] R. D. Beer, H. J. Chiel, R. D. Quinn, R. E. Ritzmann, Biorobotic approaches to the study of motor systems, Current Opinion in Neurobiology 8 (6) (1998) 777–782. doi:10.1016/S0959-4388(98)80121-9.

[75] B. Webb, What does robotics offer animal behaviour?, Animal behaviour 60 (5) (2000) 545–558. doi:10.1006/anbe.2000.1514.

[76] T. Labhart, The electrophysiology of photoreceptors in different eye regions of the desert ant, cataglyphis bicolor, Journal of Comparative Physiology A: Neuroethology, Sensory, Neural, and Behavioral Physiology 158 (1) (1986) 1–7. doi:10.1007/BF00614514.